https://doi.org/10.5194/tc-2022-129
Preprint. Discussion started: 13 July 2022

The Cryosphere Discussions

Grounding line retreat and tide-modulated ocean channels at Moscow University and Totten Glacier ice shelves, East Antarctica

Tian Li[1,2], Geoffrey J. Dawson[1], Stephen J. Chuter[1], Jonathan L. Bamber[1,2]

[1]Bristol Glaciology Centre, School of Geographical Sciences, University of Bristol, Bristol, BS8 1SS, UK
[2]Department of Aerospace and Geodesy, Data Science in Earth Observation, Technical University of Munich, Ottobrunn, 85521, Germany

Correspondence to: Tian Li (tian.li@bristol.ac.uk) and Jonathan L. Bamber (j.bamber@bristol.ac.uk)

Abstract. The Totten and Moscow University glaciers, located in East Antarctica, contain 5.1 m sea-level equivalent of ice and have been losing mass over recent decades. Using ICESat-2 laser altimetry repeat track analysis and satellite radar interferometry from Sentinel-1a/b SAR images, we mapped the grounding line locations of these two glaciers between 2017 and 2021. We detected pervasive grounding line retreat along the ice plains at the glacier central trunk of Totten Glacier Ice Shelf (TGIS) and Moscow University Ice Shelf (MUIS), where the GL retreated 3.51 ± 0.49 km and 13.85 ± 0.08 km during 1996-2020, respectively. Using CryoSat-2 radar altimetry, we found that the observed grounding line retreats are coincident with high thinning rates and high ice velocities, indicating a mass loss pattern dominated by ice dynamics. We also identified two tide-modulated ocean channels on the Totten eastern ice shelf and the Moscow University western ice shelf, where the ocean channel widths are highly correlated with the tidal range. The opening of the Moscow University western ice shelf channel connects the two previously separated TGIS and MUIS systems, which might open a pathway for the warm modified circumpolar deep water entering the main MUIS cavity and facilitate further grounding line retreat.

1 Introduction

The Antarctic Ice Sheet has contributed 7.6 ± 3.9 mm to global sea-level rise over the past 25 years (Shepherd et al., 2018). Mass loss from East Antarctica is predominantly located in Wilkes Land, which has been increasing since the 1970s (Rignot et al., 2019). Totten Glacier Ice Shelf (TGIS) and Moscow University Ice Shelf (MUIS) drain a large portion of the marine-based Aurora Subglacial Basin, which contains a sea-level rise equivalent of 5.1 m (Figure 1a) comparable to the entire West Antarctic Ice Sheet (Fretwell et al, 2013). Totten Glacier has the largest ice discharge in East Antarctica (71.4 ± 2.6 Gt yr^{-1}), with the basin it drains having the potential to raise sea level by 3.85 m (Rignot et al., 2019). With a smaller sea-level equivalent, the neighboring MUIS has an ice discharge of 47.0 ± 2.1 Gt yr^{-1} (Rignot et al., 2019). Therefore, assessing the stability of these two glaciers is important in understanding the contribution of East Antarctica to future sea level rise.

Recent evidence has recognized the critical role played by ocean forcing in both the paleo large-scale retreat of Totten Glacier during the warm Pliocene epoch (Aitken et al., 2016), and modelled future rapid retreat at the Totten eastern ice shelf

https://doi.org/10.5194/tc-2022-129
Preprint. Discussion started: 13 July 2022

grounding line (GL), the location where the grounded ice first comes into contact with the ocean and becomes afloat, through the 21st century (Pelle et al., 2021). Observations suggest that warm modified Circumpolar Deep Water (mCDW) is widespread below 500 m water depth on the Sabrina Coast continental shelf (Fig.1) (Silvano et al., 2017). Driven by nearby Dalton polynya activity, wind forcing or cyclonic eddies, the relatively warm salty water can encroach the sub-ice-shelf cavity through a deep trough (Nitsche et al., 2017), supplying sufficient heat to induce basal melting of the ice shelves (Greenbaum et al., 2015; Greene et al., 2017; Gwyther et al., 2014; Hirano et al., 2021; Rintoul et al., 2016). As a result, the TGIS and MUIS have been undergoing high basal melting compared with other regions in East Antarctica (Adusumilli et al., 2020; Depoorter et al., 2013; Pritchard et al., 2012), including at their deep GLs (Chuter and Bamber, 2015; Morlighem et al., 2020). Melting and thinning of ice shelves will reduce the buttressing of the grounded ice. If the GL is located on a retrograde bed slope, which is the case at TGIS and MUIS (Morlighem et al., 2020), it has the potential to trigger a positive feedback of increased ice discharge into the ocean through changes in ice velocity and GL positions (Joughin et al., 2014), known as the Marine Ice Sheet Instability (MISI) hypothesis (Schoof, 2007). The inland mass losses of TGIS and MUIS are concentrated in fast-flowing regions (Smith et al., 2020) and the TGIS GL retreated 1~3 km between 1996 and 2013 (Li et al., 2015), indicating a change in ice flow dynamics in response to increased ice shelf thinning likely driven by ocean thermal forcing (Khazendar et al., 2013; Li et al., 2016). Despite the importance of this region, this is the only study on GL migration of Totten Glacier from satellite observations due to the lack of available satellite data and limited spatial coverage. It is not known whether the TGIS GL has kept retreating at a similar pace as in 1996-2013, whether the GL of nearby MUIS is also retreating, or how the low-lying area between the TGIS and MUIS which is vulnerable to oceanic heat has been changing.

The high ice velocity of TGIS and MUIS limits the number of historic satellite observations of GL locations. Fast ice flow, together with katabatic wind and snowfall accumulation in this region, causes radar signal decorrelation for the Differential Synthetic Aperture Radar Interferometry (DInSAR), making it difficult to discern the GL location (Goodwin, 1990; Li et al., 2015). The satellite laser altimetry can provide supplementary GL locations where DInSAR is not available, by measuring the tidally-induced limits of ice flexure, the landward limit of tidal flexure Point F, the break-in-slope Point I_b and the inshore limit of hydrostatic equilibrium Point H. These points constitute the grounding zone (GZ), which is the transition region between the fully grounded ice sheet and the freely floating ice shelf (Fricker and Padman, 2006). The newly launched ICESat-2 satellite laser altimeter in 2018 can provide dense and high-resolution GZ locations across the Antarctic Ice Sheet (Li et al., 2022), however, its GZ measurements are not continuous in space. Therefore, combining DInSAR with satellite laser altimetry can further improve the GL coverage. In addition, studies show that tidally induced GL changes may disguise the true GL retreat signal at a sub-annual scale, therefore this effect needs to be considered when investigating the long-term GL change (Milillo et al., 2017, 2022). The relatively short repeat cycle of DInSAR data (6-day for Sentinel-1a/b) enables more detailed investigations of short-term GL migrations caused by ocean tides compared with laser altimetry (91-day for ICESat and ICESat-2). To study the GL changes of TGIS and MUIS at Wilkes Land, here we use a combination of

https://doi.org/10.5194/tc-2022-129
Preprint. Discussion started: 13 July 2022

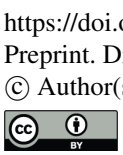

The Cryosphere
Discussions
Open Access
EGU

ICESat-2 repeat track analysis from 2019-2021 and Sentinel-1a/b DInSAR data during 2017-2021 to map the GL locations and evaluate the short-term GL variability. We then evaluate the long-term GL migrations by comparing with the historic DInSAR-derived GLs from the MEaSUREs project (Rignot et al., 2011, 2016), the ice sheet elevation change rates calculated from CryoSat-2 radar altimetry swath data (Gourmelen et al., 2018) and DInSAR-derived ice velocities (Mouginot et al., 2017b).

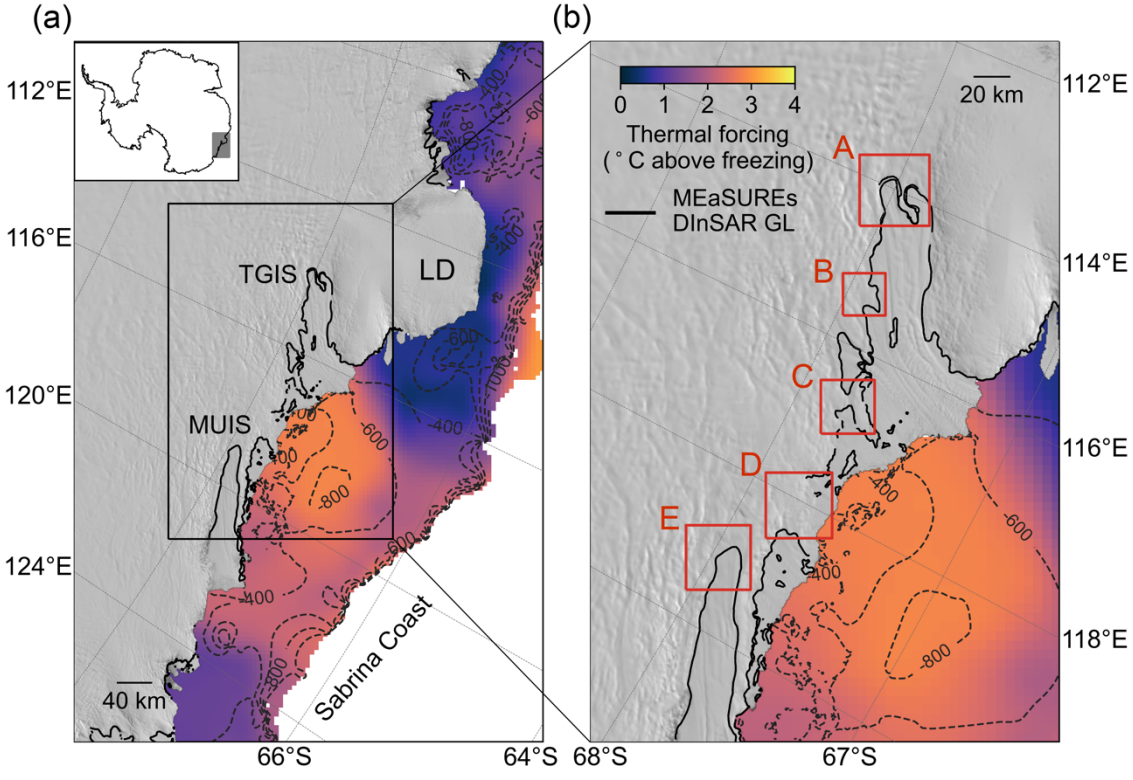

Figure 1. a) The Totten Glacier Ice Shelf (TGIS), Moscow University Ice Shelf (MUIS) and Law Dome (LD) in Wilkes Land overlaid with the MODIS mosaic of Antarctica (Scambos et al., 2007), and the maximum ocean thermal forcing (temperature above the in situ freezing point) between water depth 200-800 m (Adusumilli et al., 2020) on Sabrina Coast. The MEaSUREs Differential Synthetic Aperture Radar Interferometry (DInSAR) grounding line (GL) is shown as a black line (Rignot et al., 2011, 2016), the BedMachine bed elevation (Morlighem et al., 2020) contours at -400, -600, -800 and -1000 m of seafloor are shown as dashed dark grey lines. b) Zoomed-in map of the TGIS and MUIS outlined as the black box in a); A, B, C, D, E red boxes denote five studied regions including TGIS, TGIS East branch, TGIS East channel, MUIS West, and MUIS, respectively.

https://doi.org/10.5194/tc-2022-129
Preprint. Discussion started: 13 July 2022

2 Data and Methods

2.1 Grounding line mapping from DInSAR interferograms

To derive the GL locations of the Moscow University and Totten Glacier ice shelves in Wilkes Land, we used single look complex (SLC) synthetic aperture radar (SAR) images from both Sentinel-1a/b satellites in wide swath mode to construct DInSAR interferograms with a 6-day repeat cycle between July 2017 and September 2021. The data were processed using the GMTSAR software (Sandwell et al., 2011) and the surface topography was removed using the 8 m resolution Reference Elevation Model of Antarctica (REMA) DEM (Howat et al., 2019). We differenced the two interferograms to remove signals such as time-invariant velocity, to identify ice flow deformation signals caused by ocean tides at the GZ. We processed 139 DInSAR interferograms and manually delineated GLs according to the guidelines in Brancato et al. (2020), by counting the number of fringes between the grounded ice and the floating ice and choosing the most upstream interferometric fringe which represents the furthest point inland influenced by ocean tides. Due to poor radar signal coherence in the fast-flowing regions, we only managed to obtain three interferograms containing GL locations at the MUIS main glacier trunk and failed to derive any useful interferograms at the TGIS main glacier trunk. However, we were able to map the GLs at MUIS West, TGIS East channel and TGIS East branch ice stream. The GL delineation precision is 2 pixels, equivalent to a mapping error of approximately 90 m. In addition to the Sentinel-1a/b DInSAR-derived GLs mapped in this study, we used the historic GLs mapped from European Remote Sensing (ERS-1/2) radar satellites in 1996 and COSMO-SkyMed (CSK) constellation in 2013 as reference GLs to analyse the GL migration (Rignot et al., 2011, 2016). The deep-learning-based Antarctic GLs produced from Sentinel-1a/b SAR images in 2018 (Mohajerani et al., 2021) are also used as a reference for comparing GL migrations in this study.

2.2 Grounding zone mapping from ICESat

Brunt et al. (2010a) produced a GZ product for Antarctic ice shelves using ICESat laser altimetry datasets between 2003 and 2009. There only existed two ICESat-derived Point F locations at the MUIS main glacier trunk from the Brunt et al. (2010a) product and they were not able to map any GZ points at the main glacier trunk of TGIS. While this dataset can be used as a baseline in comparing GL change, the GZ is difficult to map in fast-flowing ice streams and can be prone to errors (Dawson and Bamber, 2017). Therefore, we reprocessed the ICESat L2 Global Antarctic and Greenland Ice Sheet Altimetry Data product GLAH12, version 34, to derive GZ information at MUIS.

The ICESat satellite was in operation between 13th January 2003 and 11th October 2009. We used the ICESat campaigns between October 2003 and October 2009 with a repeat cycle of 91 days. The release 34 dataset has been corrected for the Gaussian-Centroid (G-C) offset (Borsa et al., 2014). We applied the saturation correction to reduce the laser-energy-related impacts on elevations. To remove the elevation biases caused by long-period variations in range measurements over different

https://doi.org/10.5194/tc-2022-129
Preprint. Discussion started: 13 July 2022

mission campaigns, we applied the inter-campaign bias (ICB) corrections determined from Hofton et al. (2013) to each campaign. The ocean tide and ocean loading tide corrections were removed from the elevations as the GZ mapping requires sampling vertical elevation changes at different tidal amplitudes. We removed the data affected by clouds with the Gain Value used for Received Pulse i_gval_rcv > 200 (Bamber et al., 2009a), and removed the repeat tracks with across-track distance larger than 100 m to eliminate the across-track slope-induced errors in elevation anomaly calculation (Brunt et al., 2010b). To calculate the elevation changes caused by ocean tides at different repeat cycles, the elevations of each repeat track were interpolated to the reference orbit track with an along-track distance of 200 m. The elevation anomalies were calculated by subtracting the mean elevation of all repeat tracks on this reference track from the elevation of each repeat track profile. We obtained the elevation anomalies of track 323 across the main glacier trunk of MUIS and manually identified Point F locations (red vertical dashed lines in Fig. S1a-b, red crosses in Fig. S1c).

2.3 Grounding zone mapping from ICESat-2

The Advanced Topographic Laser Altimeter System (ATLAS) onboard ICESat-2 measures the ice surface elevation using six beams in three beam pairs with a 91-day repeat cycle (Markus et al., 2017). The across-track separation between each beam pair is about 3.3 km with a pair spacing of about 90 m. The beam pair setting allows an instantaneous determination of local across-track slopes (Smith et al., 2019). In this study, we used the Land Ice Along-Track Height Product ATL06 version 4 data (Scheick, 2019; Smith et al., 2021) from 30th March 2019 to 1st June 2021 including 9 repeat cycles (3-11), among which, cycles 4 and 11 are not complete. Our approach of processing ATL06 data and estimating the GZ features including Point F and Point H, closely follows the methodology described in Li et al. (2020, 2022). Here we briefly review the key features of this method.

The GZ mapping is based on detecting the vertical movement of floating ice caused by ocean tides, therefore we did not apply the ocean tide correction to the ICESat-2 ATL06 elevation and 're-tided' the ocean-loading tide. We categorized all the six ground tracks along each of the 1387 Reference Ground Tracks (RGTs) into nine distinct repeat-track data groups, including six single-beam repeat-track data groups and three beam-pair repeat-track data groups. For each data group, a nominal reference track was calculated, as well as a reference GL, which was the intersection between the nominal reference track and the composite GL described in Li et al. (2022). For MUIS, the reference GL was defined roughly based on the break-in-slope from the Reference Elevation Model of Antarctica (REMA) DEM (Howat et al., 2019) (white dash line in Figure S3a) to take into account different orientations of ICESat-2 tracks across the GZ and possible GL retreat during the past two decades. This ensures that no GL retreat is omitted in our study caused by the uncertainty in predefined reference GL locations on MUIS. In addition, the elevations of each repeat track in the beam-pair repeat-track data group were corrected for the across-track slope on the nominal reference track. We then calculated a set of 'elevation anomalies' by differencing each individual repeat track elevation profile and a reference elevation profile, which is defined as the average of elevations for each repeat track along the nominal reference track (Li et al., 2020, 2022).

https://doi.org/10.5194/tc-2022-129
Preprint. Discussion started: 13 July 2022

The estimation of GZ features is based on extracting the transition points from the mean absolute elevation anomaly (MAEA), which is defined as the average of the absolute value of all elevation anomaly profiles (Li et al., 2020). The limit of tidal flexure, Point F, is identified as the point where the elevation anomaly of each repeat track exceeds a noise threshold (Brunt et al., 2010b, 2011; Fricker et al., 2009), and the point where the gradient of the MAEA first increases from zero and the second derivative of the MAEA reaches its positive peak (Li et al., 2020). The point of hydrostatic equilibrium, Point H, is identified as the location where the elevation anomaly of each repeat track reaches its maximum and becomes consistent with the predictions from CATS2008 ocean tide model, which is an update to the model described by Padman et al. (2002), and the transition point where the gradient of the MAEA finally decreases to zero and the second derivative of the MAEA reaches its negative peak (Li et al., 2020).

To select the correct transition points from the second derivative of the MAEA curve as Points F and H, we used an error function fit to the MAEA as a guide to find the Point H. We then fitted an additional three-segment piecewise function to the landward part of Point H of the MAEA profile to find Point F (Li et al., 2022). The closest positive peak of the second derivative of this piecewise function to the reference GL was taken as a guide to find Point F. All results are visually inspected due to the complex nature of the GZs as a final step. In this study, we take the time stamp of the ICESat-2-derived GZ feature to be 2020, which is the median of the ICESat-2 data period used in this study.

2.4 CryoSat-2 elevation rates from swath altimetry

We used the CryoSat-2 Swath mode thematic point product from the European Space Agency (ESA) CryoTEMPO-EOLIS project (Gourmelen et al., 2018) to determine the mean rate of ice sheet elevation change ($\Delta h/\Delta t$) for the period July 2010 – December 2019 (Chuter et al., 2022). Swath processing increases the number of elevation observations by about two orders of magnitude in comparison to using standard point of closest approach (POCA) CryoSat-2 products. Before determining elevation trends, in addition to the quality filtering used in the creation of the CryoTEMPO-EOLIS product, we further reduced the potential for outliers by removing all observations with an uncertainty score > 5m. $\Delta h/\Delta t$ is determined through a linear plane fit procedure at a regular 5 km grid posting across the ice sheet:

$$z(x, y, t) = \bar{z} + a_1 x + a_2 y + a_3 xy + a_4 t + \varepsilon$$

Where z is the surface elevation, x and y are the spatial coordinates, t is time and ε is the observation noise. The coefficients a_1, a_2 and a_3 resolve for variations in ice sheet surface topography within each grid cell. Due to swath elevation data typically having a larger noise level than conventional POCA products (Gray et al., 2017), an iterated re-weighted least squares approach was used, with model fit residuals > 2σ removed after each iteration until no residual outliers remained.

Additionally, the grid cells resulted from the potentially poorly fitted planes were removed if any of the following conditions were met: an absolute $\Delta h/\Delta t$ > 15 m yr^{-1}, surface slope > 3° and a plane fit uncertainty > 1 m yr^{-1}. In addition, a 50 km kernel

https://doi.org/10.5194/tc-2022-129
Preprint. Discussion started: 13 July 2022

Median Absolute Deviation (MAD) filter was used to remove Δh/Δt values which have a value > 2 MAD. Finally, a 15 km median filter was applied to reduce any artifacts of the gridded values.

2.5 Height above hydrostatic equilibrium

To calculate the height above hydrostatic equilibrium, we used the ice-equivalent ice thickness H and surface elevation h referenced to mean sea level available from the BedMachine Antarctica dataset (Morlighem, 2020; Morlighem et al., 2020):

$$h_f = h - H\frac{(\rho_w - \rho_i)}{\rho_w}$$

The sea water density ρ_w and ice density ρ_i are 1,027 kg m^{-3} and 917 kg m^{-3}, respectively. The nominal error is 11 m based on the uncertainty of 2 m in surface elevation and 100 m in bed topography.

2.6 Other datasets

Two different tide models CATS2008 (Padman et al., 2002) and FES2014 (Lyard et al., 2021) are used to check the tidal range at each DInSAR GL measurement. To study the ice velocity changes at the GZs, we used the MEaSUREs annual ice velocity maps with a 1 km grid spacing, version 1, between 2005 and 2016 (Mouginot et al., 2017a, 2017b). This dataset is derived from a combination of InSAR-based analysis of multiple SAR data and the feature tracking of Landsat-8 images. For ice velocities between 2017 and 2018, we used the ITS_LIVE annual ice velocity datasets derived from Landsat optical images using features tracking (Gardner et al., 2018, 2019). We used the circum-Antarctic iceberg calving dataset (Qi et al., 2021) to calculate the annual cumulative iceberg calved area at the calving fronts of Moscow University and Totten Glacier Ice Shelves. This dataset records every independent calving event larger than 1 km^2 for all the Antarctic ice shelves between 2005 and 2018 derived from multisource optical and synthetic aperture radar (SAR) images.

3 Results

3.1 Grounding line migration in fast-flowing areas

3.1.1 Moscow University Ice Shelf

The only publicly available historic measurements of Point F with full spatial coverage at the main glacier trunk of MUIS, is the 1996 ERS-1/2 DInSAR-derived GL from the MEaSUREs project (Rignot et al., 2011, 2016). However, we cannot replicate this interferogram due to the lack of available Level 1 ERS-1/2 SAR Simple Look Complex data in 1996 in this region. Nevertheless, the elevation anomaly analysis of ICESat repeat tracks along RGT 323 (Fig. S1) between June 2004

https://doi.org/10.5194/tc-2022-129
Preprint. Discussion started: 13 July 2022

and November 2005 in our study matches well with the 1996 GL. It identifies an erroneous geolocation of Brunt et al. (2010a)'s ICESat-derived Point F at the eastern flank of the MUIS GZ (purple cross in Figure S1c). The proximity between the 1996 GL and newly derived ICESat Points F along RGT 323 gives us confidence that the 1996 GL is accurate and reliable, and we use, therefore, the 1996 GL as a baseline to evaluate the GL migration rates in this region. However, the RGT 323 is the only ICESat ground track available at the MUIS GZ and it is not situated on the main glacier trunk. It is important to note that large uncertainties might exist for the MEaSUREs GL in 1996 due to tidal amplitude variations (Milillo et al., 2017) in areas not covered by the ICESat repeat tracks.

Three Sentinel-1a/b DInSAR interferograms with a 6-day repeat cycle between 23rd April and 5th May 2021 (Figs. 2b-d) show a rapid short-term GL migration of 2.53 ± 0.13 km in just six days (Table S4). A high positive correlation is found between the GL migration distance and the absolute tidal range |dh| with an R-squared value of 0.99 (Fig. 3), indicating this short-term GL fluctuation is likely driven by ocean tides. Compared with the 1996 GL, the furthest GL migration inland along the ice flowline among these three interferograms is 5.67 ± 0.13 km, and the average GL retreat of these three DInSAR interferograms is 4.22 km with a standard deviation of 1.07 km. The variation in GL location caused by short-term ocean tides is shorter than the smallest GL migration of 3.14 km on April 23rd 2021 since 1996. Assuming that the tide-induced GL fluctuation range is constant over time, this indicates that the observed GL migration from DInSAR includes a long-term trend.

To supplement the limited Sentinel-1a/b DInSAR measurements, we calculated the elevation anomalies of repeat tracks along four different RGTs of ICESat-2 laser altimetry data (163, 841, 1108 and 1283) across the same region, to derive Point F locations (red dots in Figure 2a and vertical red dashed lines in Figure 4). Ten ICESat-2-derived Point F locations at the southernmost portion of the MUIS GZ were selected to calculate the GL migrations along the ice flowlines (Fig. S3a) by comparing with the 1996 DInSAR GL. The average GL retreat distance at the western flank of MUIS GZ is 13.85 km, while it is 9.37 km at the eastern flank of the MUIS GZ (Table S1). Large GL deviations (~5.9 km along ice flowline, Fig. 2a) exist between the ICESat-2-derived Point F at Track 1108 GT2R (8 March – 7 June 2020) (Fig. 4a) and the Sentinel-1a/b DInSAR GL on 29th April 2021 (Fig. 2c). One possible explanation for this deviation is short-term GL fluctuations caused by different ocean tidal amplitudes that are not fully captured in our study.

The Sentinel-1a/b DInSAR interferograms in June 2018 show the existence of an oval-shaped feature at the southeast flank of the MUIS GZ (Figs. 2e,f), which was previously detected as a GL in Mohajerani et al. (2021). This oval-shaped feature is not constant over time on the interferogram, disappearing in September 2021 with another similar oval-shaped feature appearing in the north (Fig. 2g). By analyzing the repeat tracks of three ICESat-2 ground tracks RGT 163 GT2L (Fig. S5), RGT 338 GT2R (Fig. S6) and RGT 605 GT3L (Fig. S7), we found that the two unusual lobate-shaped features are probable subglacial lakes. The ICESat-2 elevation anomaly time series of tracks 163 and 338 show gradual surface uplift between 20 April 2019 (cycle 3) and 14 October 2021 (cycle 13) on the southern lake, with a height change up to 10 m (Fig. S6). In the

https://doi.org/10.5194/tc-2022-129
Preprint. Discussion started: 13 July 2022

meantime, track 605 shows a similar uplifting event between 3 May 2021 (cycle 11) and 1 November 2021 (cycle 13) on the northern lake, and the height change is around 2 m during this period (Fig. S7).

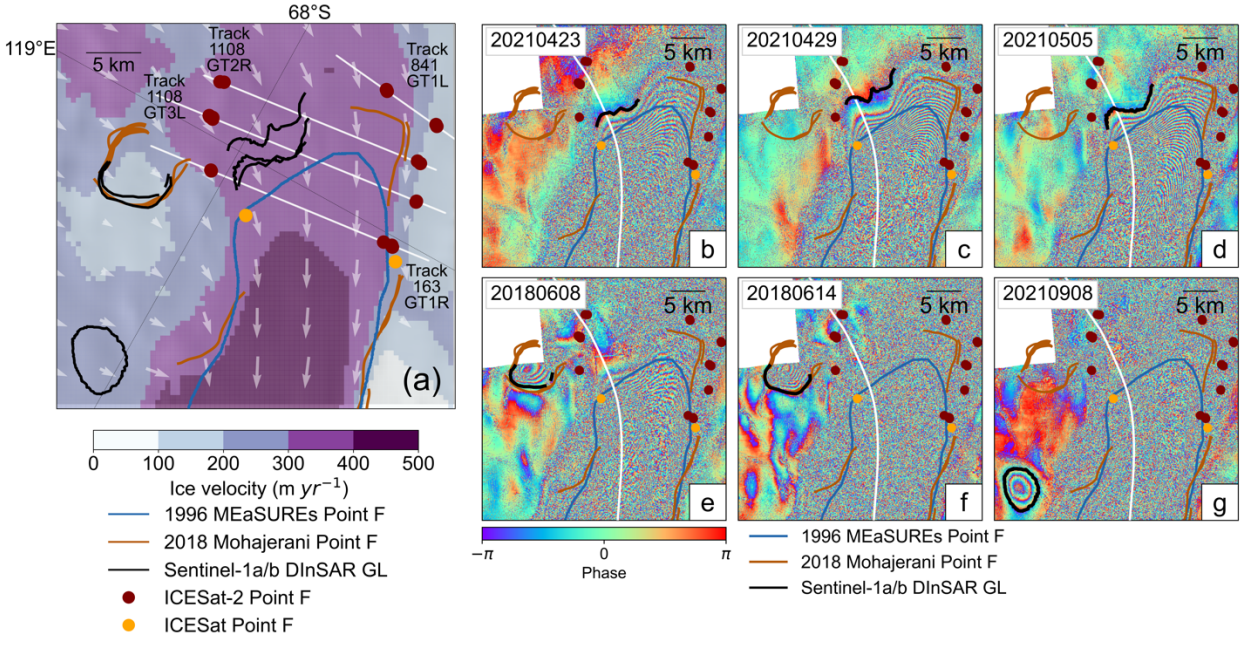

Figure 2. a) Grounding line (GL) distributions at the main glacier trunk of the Moscow University Ice Shelf (MUIS) overlaid with the ice surface velocity magnitudes and ice flow directions (white arrows) (Rignot et al., 2017). The ICESat-2-derived inland limit of tidal flexure (Point F) locations are shown as red dots, and the ICESat-derived Points F locations from Figure S1 are shown as orange dots. b-g) Sentinel-1 DInSAR interferograms of the MUIS between 2018 and 2021. In all subplots, the 1996 MEaSUREs DInSAR GL (Rignot et al., 2011, 2016) and the 2018 DInSAR GL (Mohajerani et al., 2021) are shown as blue solid line and brown solid line, respectively. The GLs delineated from Sentinel-1a/b DInSAR interferograms in our study are shown as black solid lines in each subplot.

https://doi.org/10.5194/tc-2022-129
Preprint. Discussion started: 13 July 2022

The Cryosphere
Discussions
Open Access
EGU

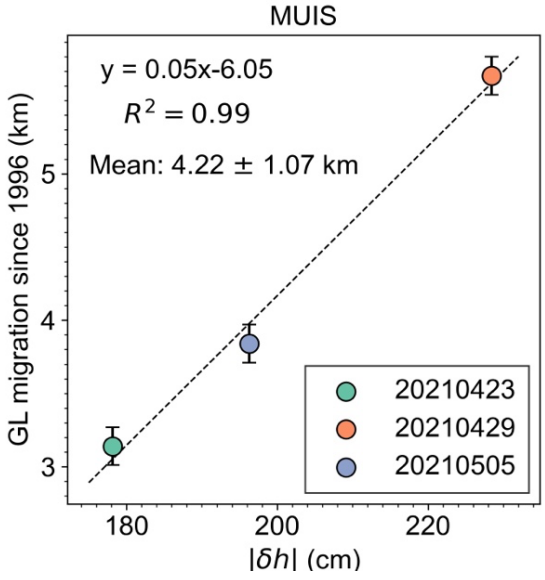

235

Figure 3. Correlation between the absolute tidal range calculated from the CATS2008 tidal model at the acquisition dates of each interferogram and the grounding line migrations since 1996 for the three Sentinel-1a/b DInSAR interferograms in Figures 2b-d (Table S4). The grounding line migration is measured along the ice flowline (white solid line in Figures 2b-d).

https://doi.org/10.5194/tc-2022-129
Preprint. Discussion started: 13 July 2022

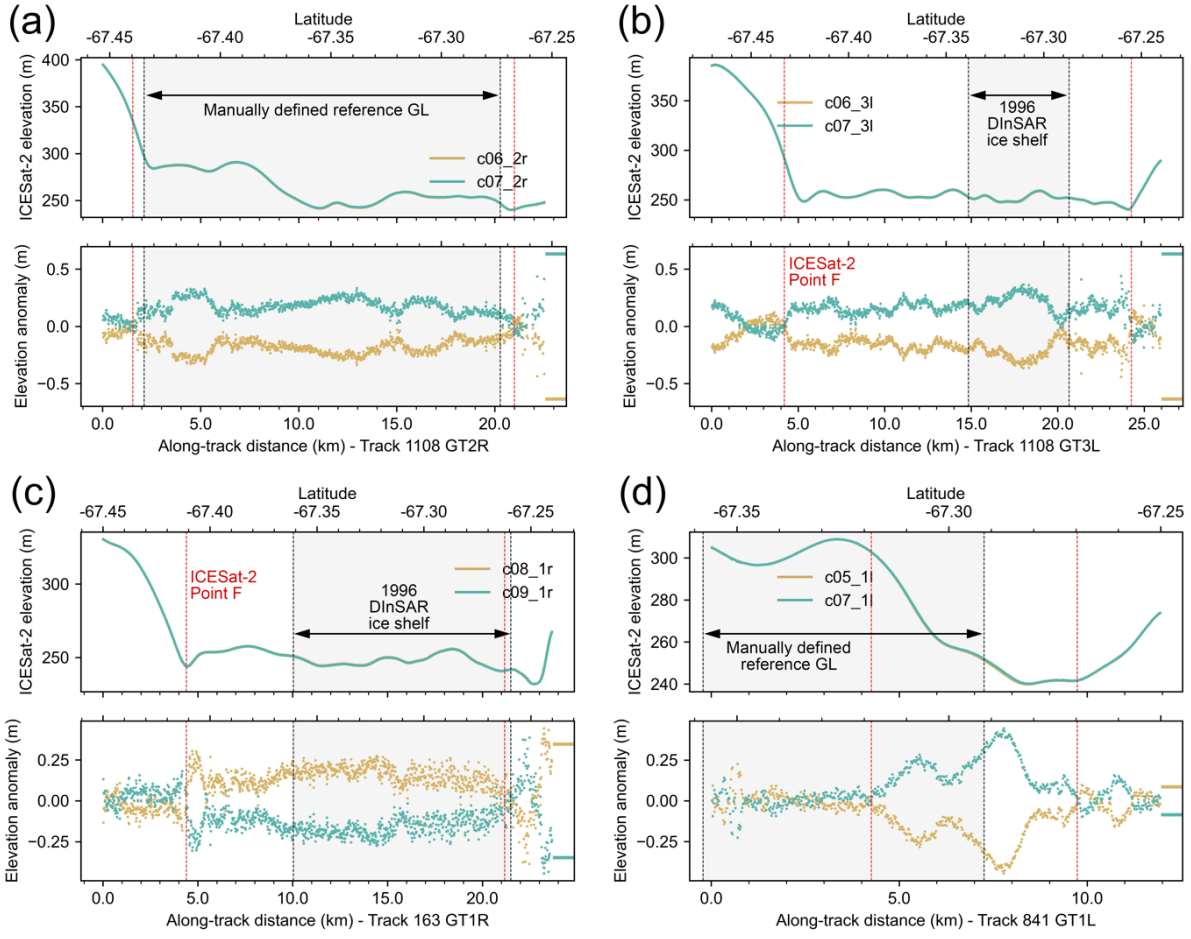

240 **Figure 4. The ICESat-2 elevation anomaly analysis for different elevation profiles on the main glacier trunk of Moscow University Ice Shelf (MUIS) shown in Figure 2a, including track 1108 GT2R (a), track 1108 GT3L (b), track 163 GT1R (c) and track 841 GT1L (d). For all subplots, the upper panel shows the surface elevation and the lower panel shows the elevation anomalies, the ICESat-2-derived Point F is shown as the vertical red dashed line, the zero mean ocean tidal amplitudes predicated from the CATS2008 tidal model at the location of -67.0714° S, 120.6249° E are shown as the horizontal line segments on the right side of the**
245 **plot.**

3.1.2 Totten Glacier Ice Shelf

High ice velocity at the fast-flowing TGIS main glacier trunk and the 6-day repeat cycle for Sentinel-1a/b satellites cause a loss of phase coherence in all Sentinel-1a/b DInSAR interferograms. Therefore, no GLs can be reliably detected from Sentinel-1 DInSAR measurements at the TGIS main glacier trunk in our study. With ICESat-2 repeat tracks, however, we
250 were able to identify the GZ locations at the southern lobe of the TGIS (red dots in Figure 5a). Four examples of the ICESat-2 repeat track analysis for track 1207 GT2R, track 1207 GT3L, track 1032 GT1L and track 1032 GT2R are shown in Figure

https://doi.org/10.5194/tc-2022-129
Preprint. Discussion started: 13 July 2022

S2. The historic GLs in 1996 and 2013 in this region were mapped with high confidence according to Figure 2 in Li et al. (2015), therefore they were used as a reference in calculating GL migration rates with ICESat-2-derived Point F locations along the ice flowlines shown in Figure S3b.

The GL migration and retreat rates at the southern lobe of the TGIS between 1996 and 2020 are listed in Table S2. During 2013-2020, the GL retreated 0.75 ~ 2.33 ± 0.1 km which is equivalent to an average retreat rate of 0.11 ~ 0.33 km yr^{-1}. In comparison, the GL retreated 1.93 ~ 2.17 ± 0.1 km during 1996-2013, equivalent to an average GL retreat rate of 0.11 ~ 0.13 km yr^{-1}. In addition to calculating GL migration rates, we investigated the short-term variation in GLs modulated by ocean tides (Fig. 5b). We directly measured the tidal amplitudes from the ICESat-2 elevation anomalies at Point H for each GZ measurement. Given that the chosen ICESat-2-derived Points F are close in geolocations and the corresponding ice flowlines are near parallel at the GZ (Fig. S3b), deviations in GL migration caused by spatial discrepancy in ice flowline locations should be small. A high correlation between GL migration and tidal range with an R-squared value of 0.71 was found. The average GL migration is 3.51 km between 1996 – 2020, and the standard deviation is 0.49 km which was taken as the spatial variation caused by the short-term tidal amplitude changes during this period.

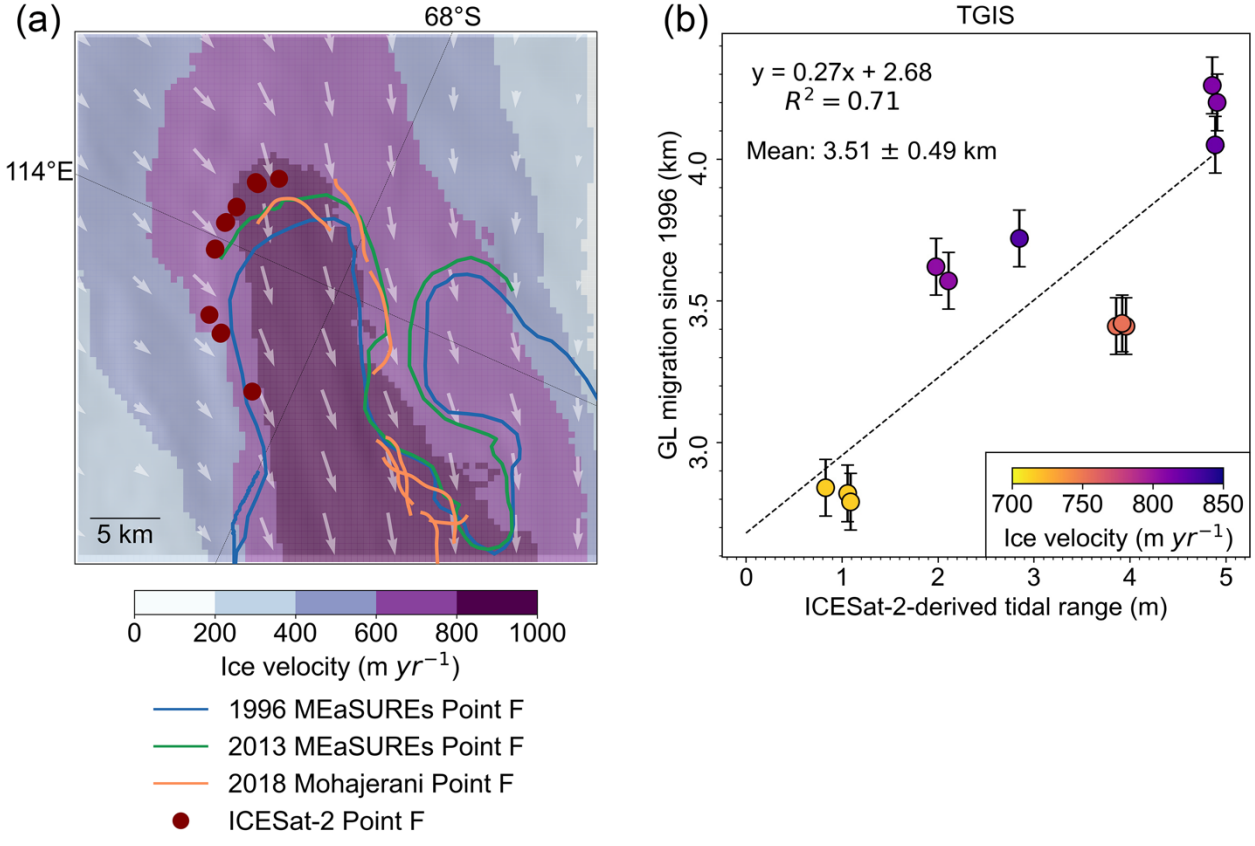

https://doi.org/10.5194/tc-2022-129
Preprint. Discussion started: 13 July 2022

Figure 5. a) Grounding line (GL) distributions at the main glacier trunk of the Totten Glacier Ice Shelf (TGIS) overlaid with the ice surface velocity magnitudes (Rignot et al., 2017) and ice flow directions (white arrows). The ICESat-2-derived Points F are shown as red dots. The 1996 and 2013 DInSAR-derived GLs (Rignot et al., 2011, 2016) are shown as blue and green solid lines, respectively. The 2018 DInSAR-derived GLs (Mohajerani et al., 2021) are shown as orange solid lines. b) The ICESat-2-derived tidal range for each Point F at the selected ice flowlines in Figure S3b and the GL migration distance between DInSAR-derived GL in 1996 (Rignot et al., 2011, 2016) and ICESat-2-derived Point F in 2020 along ice flow.

3.1.3 Totten East branch

Located at the eastern flank of TGIS, the Totten East branch is a relatively fast-flowing ice stream with an ice velocity of about 200 m yr^{-1}. Eleven Sentinel-1a/b DInSAR interferograms between 2018 and 2021 in Figure 6 show that the GL has been retreating since 1996 (Table S5). The GL retreat distances along the same ice flowline (orange line in Figure 6a) vary between 4.64 ~ 6.96 ± 0.13 km. In addition, we calculated a mean GL retreat distance to be 5.95 km from DInSAR interferograms, and the standard deviation is 0.75 km. In contrast to MUIS and TGIS main glacier trunks (Figs. 3 and 5b), no positive correlation was found between the tidal ranges calculated from the CATS2008 tidal model and the GL retreat distances (Fig. 7). Although it is unclear if this lack of uncorrelation is caused by an inaccurate tidal model prediction in this region, different fringe numbers of each interferogram (Fig. 6) indicate a variation in ocean tidal amplitudes which can change the GL shape at the chosen ice flowline as well as the final GL migration distances. In addition, the fact that the magnitude of short-term GL fluctuations (0.75 km) is much smaller than the mean GL migration distance since 1996 indicates that the observed landward GL migrations are mainly long-term GL retreat.

https://doi.org/10.5194/tc-2022-129
Preprint. Discussion started: 13 July 2022

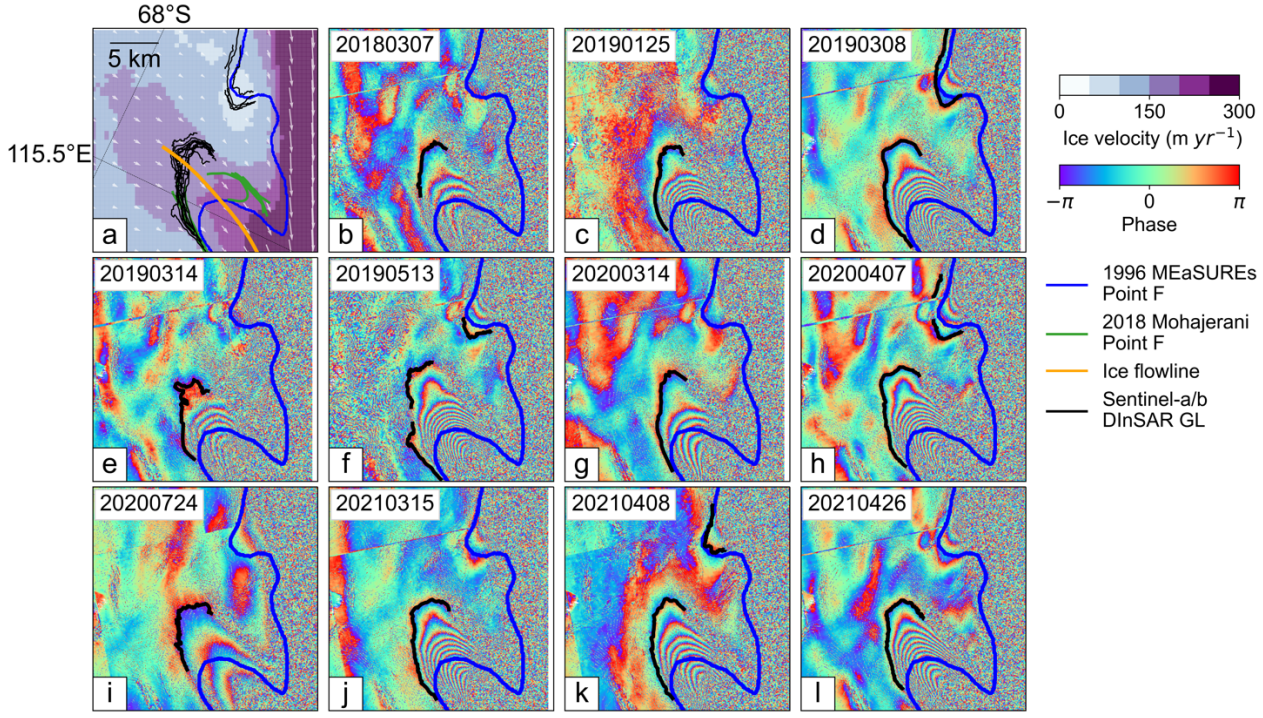

285 **Figure 6. a) Distribution of different grounding line (GL) products at the Totten East branch overlaid with the ice surface velocity magnitudes (Rignot et al., 2017) and ice flow directions (white arrows). b-k) GLs (black solid line) delineated using Sentinel-1a/b DInSAR interferograms between 2018 and 2021. In all subplots, the 1996 DInSAR-derived GL (Rignot et al., 2011, 2016) and 2018 DInSAR-derived GL (Mohajerani et al., 2021) are shown as blue solid line and green solid line, respectively. The ice flowline used to measure the GL migration rates is shown as the orange solid line in subplot a).**

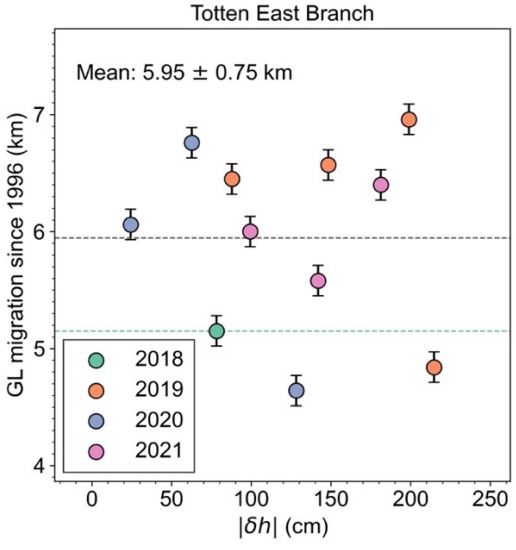

290

https://doi.org/10.5194/tc-2022-129
Preprint. Discussion started: 13 July 2022

Figure 7. Comparison between the grounding line (GL) migration and tidal range |dh| from the CATS2008 tidal model, at the times of each DInSAR scene at the Totten East branch. Positive GL migration values indicate that the GL retreated inland with respect to the reference point, which is the intersection between the 1996 DInSAR-derived GL (Rignot et al., 2011, 2016) and the ice flowline in Figure 6a. The grey horizontal dashed line denotes the mean GL retreat distance, the green horizontal dashed line is the GL migration distance on March 7th, 2018 in Figure 6b.

3.2 Tide-modulated ocean channels

Sentinel-1a/b DInSAR interferograms at the low-lying areas of the TGIS and MUIS show there are two ocean tide modulated channels, one located at the Totten eastern ice shelf (Fig. 8, box C in Fig. 1b) and the other located at the Moscow University western ice shelf (Fig. 9, box D in Fig. 1b). Previous research using radar sounding data and laser altimetry datasets discovered the existence of an ocean trough at the Totten eastern ice shelf (Greenbaum et al., 2015). This enables an easier entry of warm mCDW into the main TGIS cavity. Similarly, the Sentinel-1a/b DInSAR interferograms in our study show the existence of this channel (Fig. 8). From these interferograms, we observe that the channel width is not constant, but correlated with the tidal range with an R-squared value of 0.66 (Fig. 10a). For example, when ocean tides were low, the channel was completely closed (Figs. 8b, 8e, 8j and 8m). When the ocean tide range increased from 17th April to 29th April 2021, the channel reopened and its width increased to 2.89 ± 0.13 km (Table S7). In Greenbaum et al. (2015), they claimed it is difficult to determine whether this channel formed recently, or formed before 1996 but the ERS-1/2 DInSAR interferogram failed to capture the correct tidal signal due to radar signal coherence issues. The results here support a third possibility, the 1996 ERS-1/2 DInSAR-derived GL is accurate but the ERS satellite passes happened to be at low tide when the channel was closed. We calculated the absolute tidal range at the acquisition times of the ERS-1/2 SAR images used in the MEaSUREs 1996 DInSAR-derived GL over this cavity (Rignot et al., 2016), which is 8.6 cm from CATS2008 (vertical orange dotted line in Figure 10a) or 9.77 cm from FES2014 tidal model (Table S3). According to the linear regression in Figure 10a, the channel width should be close to zero at this tidal range.

Another example of a tide-modulated ocean channel is located at the Moscow University western ice shelf. On 17th April 2021, the Western MUIS channel was closed due to low tides (Fig. 9e, Table S6). Then its width expanded to 2.84 ± 0.13 km on 29th April (Fig. 9g) in just 12 days (Table S6). According to Figure 10b, the channel width is positively correlated with the tidal range with an R-squared value of 0.49, lower than the Totten eastern ice shelf channel. The most likely causes of this lower correlation coefficient are that we have fewer DInSAR observations in this region which resulted in fewer data samplings, and the fact that ice over a narrower ocean trough might not deflect adequately in hydrostatic equilibrium compared to a wider trough such as the case in Totten eastern ice shelf. Due to a loss of coherence in the Sentinel-1a/b DInSAR interferograms, we are unable to map the GL locations at most of the southern region of the Moscow University western ice shelf (Fig. 9). Despite this, the opening of this ocean channel indirectly confirms that the GL has retreated further inland to the channel entry. This is also supported by the DInSAR GL observation on 5th May 2021 in Figure 9h (black line) on the ice shelf southern GZ. The GL migration distance along an ice flowline (red line in Figure 9a) between 5th May 2021

https://doi.org/10.5194/tc-2022-129
Preprint. Discussion started: 13 July 2022

and 1996 is 11.95 ± 0.13 km, equivalent to an average retreat rate of 0.48 km yr^{-1}. As this is the only Sentinel-1a/b DInSAR interferogram that contains a GL signal at the southern flank of the MUIS western ice shelf, the possibility of short-term GL fluctuations caused by ocean tides cannot be ruled out. However, the ESA CCI DInSAR GL location in 1996 (ESA, 2017) (red line in Fig. S4d) mapped from ERS-1/2 SAR images matches well with the MEaSUREs GL in this region (orange line in Fig. S4d). This suggests that the large GL migration in this region is dominated by a long-term trend and not the short-term tidal variability.

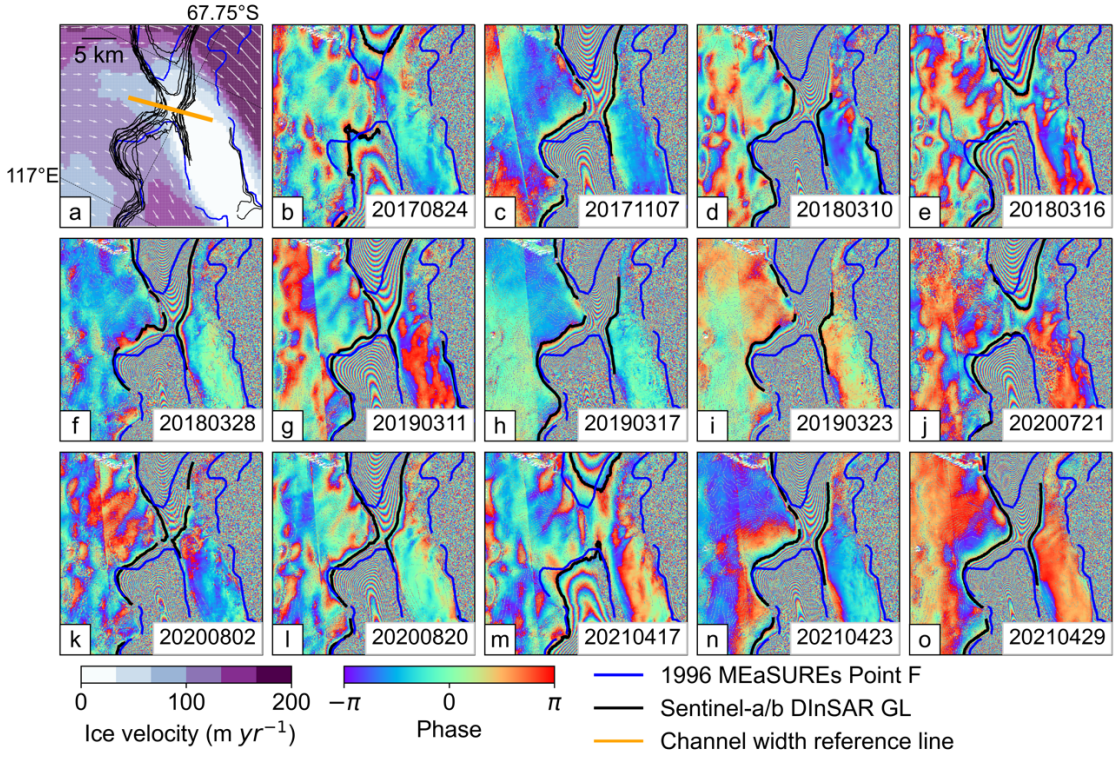

Figure 8. a) Distribution of different grounding line (GL) products at the Totten eastern ice shelf channel overlaid with the ice surface velocity magnitudes (Rignot et al., 2017) and ice flow directions (white arrows). The orange line is the reference line for measuring channel width. b-o) GLs (black solid line) delineated using Sentinel-1a/b DInSAR interferograms between 2017 and 2021. In all subplots, the 1996 DInSAR-derived GL (Rignot et al., 2011, 2016) is shown as blue solid line.

https://doi.org/10.5194/tc-2022-129
Preprint. Discussion started: 13 July 2022

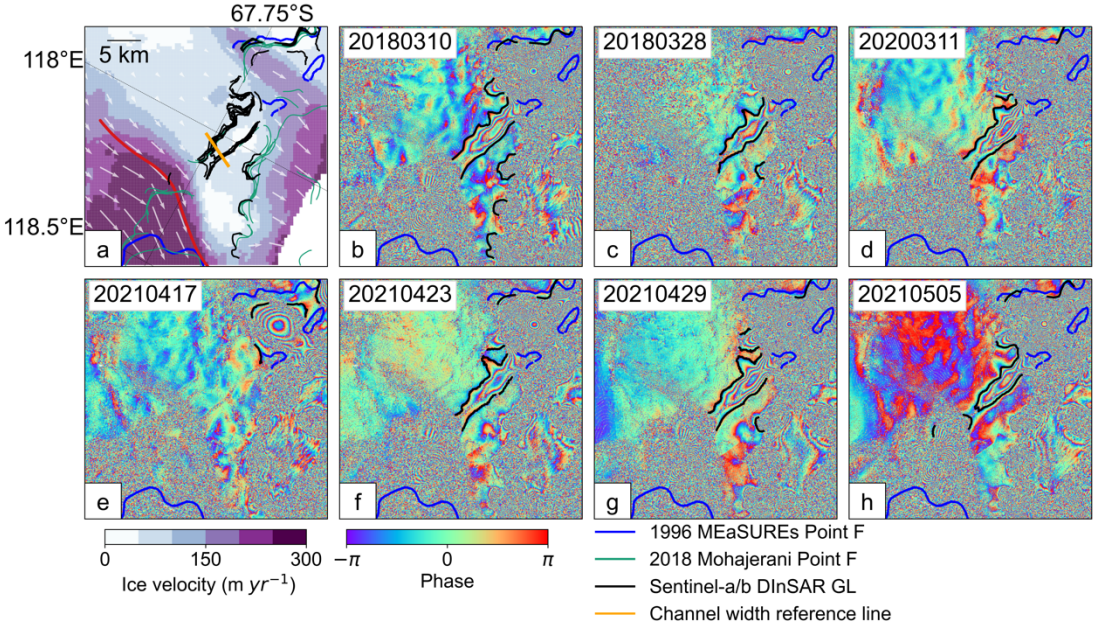

335

Figure 9 a) Distribution of different grounding line (GL) products at the Moscow University western ice shelf channel overlaid with the ice surface velocity magnitudes (Rignot et al., 2017) and ice flow directions (white arrows). The orange line is the reference line for measuring channel width. b-h) GLs (black solid line) delineated using Sentinel-1a/b DInSAR interferograms between 2018 and 2021. In all subplots, the 1996 DInSAR-derived GL (Rignot et al., 2011, 2016) and 2018 DInSAR-derived GL
340 **(Mohajerani et al., 2021) are shown as blue solid line and green solid line, respectively. The ice flowline used to measure the GL migration rates is shown as the red solid line in subplot a).**

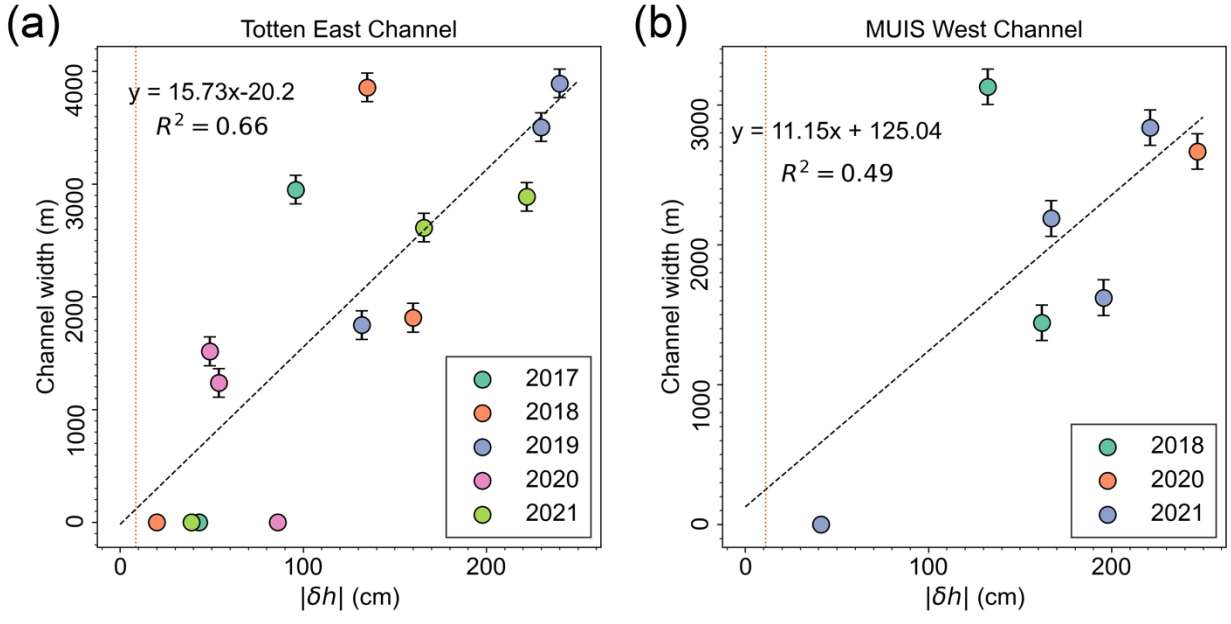

https://doi.org/10.5194/tc-2022-129
Preprint. Discussion started: 13 July 2022

Figure 10. a) Comparison between the absolute values of the modelled tide range |δh| using the CATS2008 tidal model at the location of -67.0131° S, 117.0389° E, and the width of Totten eastern ice shelf channel (Table S7). Year acquisition of DInSAR data is colour-coded shown in the legend. The channel width is measured using the reference line shown as the orange line in Figure 8a. b) Comparison between the absolute values of the modelled tide range |δh| using the CATS2008 tidal model at the geolocation of -67.1023° S, 117.7366° E, and the width of Moscow University western ice shelf channel (Table S6). Year acquisition of DInSAR data is colour-coded, the channel width is measured using the reference line shown as the orange line in Figure 9a. In both subplots, the vertical orange dotted lines denote the absolute tidal ranges from the CATS2008 tidal model at the time of the satellite passes used in MEaSUREs 1996 ERS-1/2 DInSAR grounding line measurements in each region (Rignot et al., 2011, 2016) (Table S3).

3.3 Hydrostatic potential and ice thinning

The GL migrations at the five studied regions across Wilkes Land (Table 1) are happening in areas with high hydrostatic potential, where the ice is only grounded a few tens of meters above hydrostatic equilibrium (Fig. 11). These areas are prone to rapid GL retreat with only a small amount of ice thinning (Li et al., 2015) and large short-term GL fluctuations due to ocean tide variations (Brunt et al., 2011; Milillo et al., 2017). Four distinct regions among those studied, including the MUIS, TGIS, TGIS East branch and MUIS West, are in fast-flowing regions with an ice velocity higher than 200 m yr^{-1}. In addition, CryoSat-2 surface elevation change rates during 2010-2019 (Fig. 12) show strong thinning signals at the fast-flowing regions upstream of the GZs at MUIS, TGIS and TGIS East branch. The highest elevation change rates on the central trunk of MUIS, TGIS and TGIS East branch are -0.9 ± 0.01 m yr^{-1}, -1.64 ± 0.01 m yr^{-1} and -0.72 ± 0.02 m yr^{-1}, respectively. The elevation change due to firn and SMB processes is less than 0.16 m yr^{-1} between 2010 and 2016 based on the RACMO 2.3 Firn Densification Model (FDM) (Kuipers Munneke et al., 2015; Melchior Van Wessem et al., 2018). Therefore, it is likely that the surface elevation change is predominantly caused by dynamical thinning. The bed topography underneath MUIS and TGIS main glacier trunks near the GL is 2000 ~ 2300 below sea level (Figs. S4a-b). For TGIS, the bed topography remains nearly level along the southern lobe (Fig. S4b). For the western flank of the MUIS main glacier trunk (Fig. S4a), the TGIS East branch (Fig. S4c) and the MUIS West (Fig. S4d), the bed elevation decreases further inland, and the GLs have been retreating along retrograde bed slopes.

Zero mean annual ice velocity changes and the annual cumulative iceberg calved areas between 2005 and 2018 at six different GZ sites (red box in the grey inset of each subplot) are shown in Figure 13. At the MUIS GZ (Figs. 13a-b), the ice velocities increased from 2007 to 2010 by about 50 m yr^{-1} and remained stable until 2016. The ice velocity acceleration during 2007-2010 was only accompanied by small calving events with an annual calving area less than 50 km^2 (grey boxes in Figures 13a-b), indicating the ice velocity change might be caused by ice thinning and associated GL retreat at MUIS. For the southern TGIS, the ice velocity first increased from 2005 to 2007 by 51 m yr^{-1}, kept stable with a slight decrease of 9 m yr^{-1} until 2016, then decreased 102 m yr^{-1} in 2017. At the TGIS East branch, where an average 5.95 km GL retreat was observed during 1996-2020, ice velocity firstly decreased from 2005 to 2007, then increased about 40 m yr^{-1} until 2018. For

https://doi.org/10.5194/tc-2022-129
Preprint. Discussion started: 13 July 2022

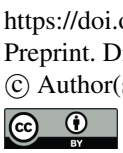

the MUIS West channel and the TGIS East channel, the ice velocities at the GZ have been stable between 2005 and 2018, with an ice velocity variation less than 30 m yr^{-1}.

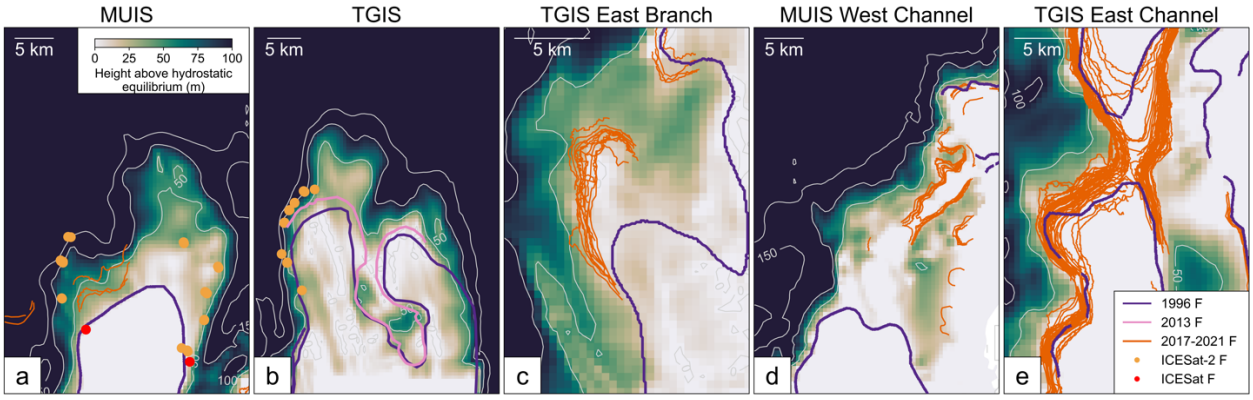

Figure 11. Height above hydrostatic equilibrium in Moscow University Ice Shelf (MUIS) main glacier trunk (a), Totten Glacier Ice Shelf (TGIS) main glacier trunk (b), Totten East branch ice stream (c), Moscow University western ice shelf ocean channel (d), and Totten eastern ice shelf ocean channel (e).

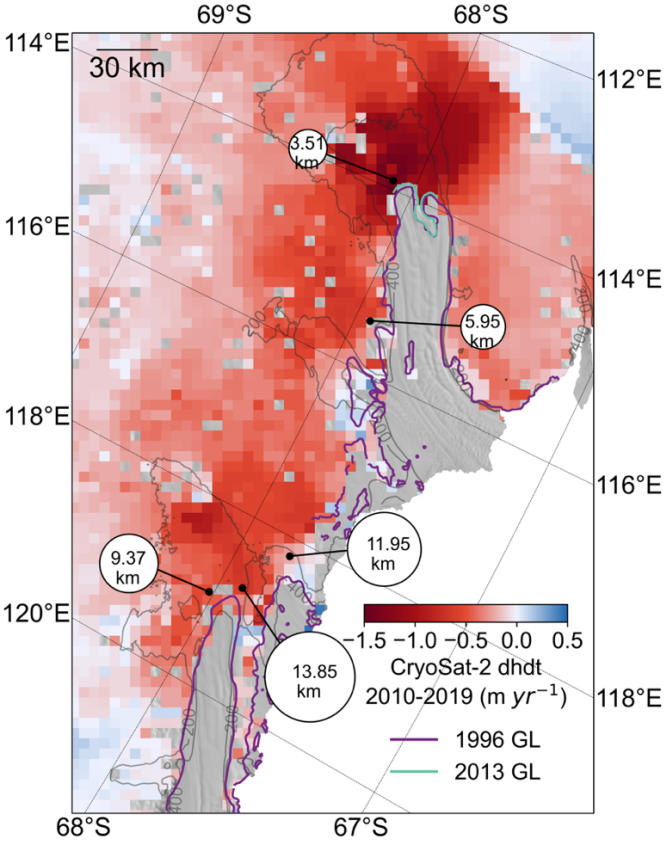

https://doi.org/10.5194/tc-2022-129
Preprint. Discussion started: 13 July 2022

Figure 12. CryoSat-2 surface elevation change rate between 2010 and 2019 on grounded ice overlaid with the grounding line retreat distance measured in this study since 1996 (Table 1).

385 **Table 1. The mean grounding line (GL) migration distance and standard deviation in five studied regions including MUIS eastern flank, MUIS western flank, MUIS West ice shelf, TGIS East branch and the TGIS southern lobe.**

Region	Time Period	Instrument	Mean GL Migration (km)	Standard Deviation (km)
MUIS eastern flank	1996-2020	ICESat-2	9.37	1.04
MUIS western flank	1996-2020	ICESat-2	13.85	0.08
MUIS West ice shelf	1996-2021	Sentinel-1a/b	11.95*	-
TGIS East branch	1996-2020	Sentinel-1a/b	5.95	0.75
TGIS southern lobe	1996-2020	ICESat-2	3.51	0.49

***Note at the MUIS West ice shelf, there is only one present-day Sentinel-1a/b DInSAR interferogram available for measuring the GL migration distance.**

https://doi.org/10.5194/tc-2022-129
Preprint. Discussion started: 13 July 2022

The Cryosphere
Discussions
Open Access
EGU

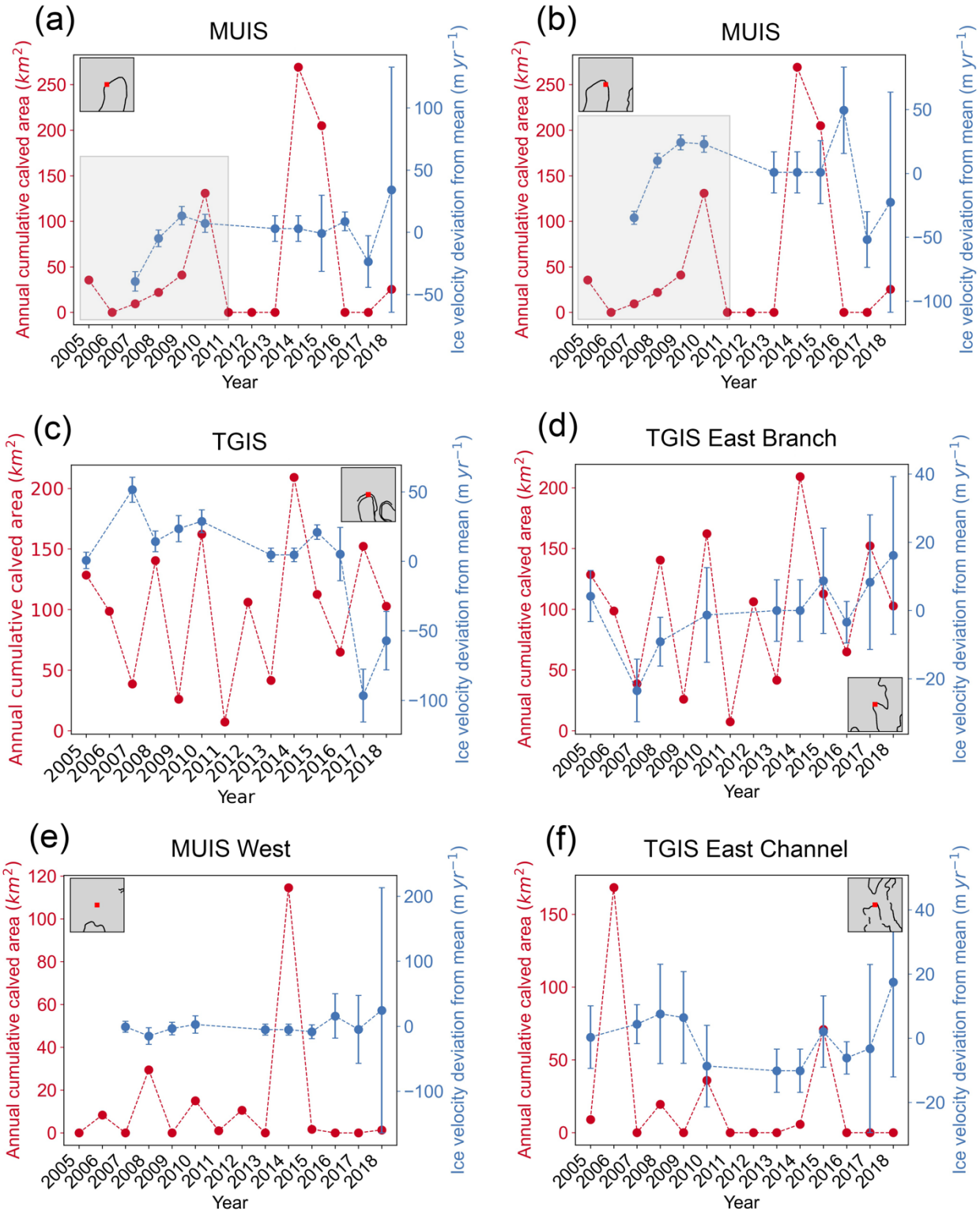

https://doi.org/10.5194/tc-2022-129
Preprint. Discussion started: 13 July 2022

Figure 13. The ice velocity time series at each grounding zone (red box in the grey inset map) derived from MEaSUREs (2005-2016) (Mouginot et al., 2017a, 2017b) and ITS_LIVE (2017-2018) (Gardner et al., 2018, 2019) annual ice velocities, and the annual cumulative iceberg calved area at the ice shelf front (Qi et al., 2021).

4 Discussion

The southern lobe of TGIS retreated at a mean rate of 0.21 km yr^{-1} in 2013-2020, higher than the 0.12 km yr^{-1} mean retreat rate in 1996-2013 mapped by Li et al. (2015) (Table S2). Although the ice velocity at the southern lobe of TGIS maintained stable between 2007-2016 and showed a slowdown in 2017 (Fig.13c), the mass loss of TGIS has increased through the period of 1979-2017 and remained at about 10% of the balance flux (Li et al., 2016; Rignot et al., 2019). This would indicate a continuous GL retreat at the fast-flowing region of TGIS. Note we only managed to map the GZ at the eastern flank of the TGIS southern lobe where the bed elevation is increasing inland along the ice flowlines (Fig. S3b and S4b), this might not represent the overall GL retreat rates over this region despite having the highest negative elevation rates derived from CryoSat-2 radar altimetry (Fig. 12)

Sentinel-1a/b DInSAR interferograms show that GL retreat also happened at the TGIS East branch with a mean rate of 0.25 km yr^{-1} from 1996-2020 (Fig. 7), the GL migration trend in this region is similar to modelled results on Totten Glacier evolution through 2100 (Pelle et al., 2021). Our average retreat rate is almost ten times the highest GL retreat rate of 0.027 ± 0.016 km yr^{-1} during 2010-2016 calculated by Konrad et al. (2018) in this region. The GL retreat at the TGIS East branch happened along a retrograde bed slope (Fig. S4c), coincided with high ice velocity (Fig. 6a) and negative elevation change in this region (Fig. 12). Moreover, the ice velocity at the GZ has been increasing moderately since 2007 (Fig. 13d). This behavior suggests the possibility of MISI taking place in this sector and the GL retreat possibly occurred during the past decade.

Although we are unable to duplicate the DInSAR interferogram at the main glacier trunk of MUIS in 1996, the ICESat repeat track analysis along RGT 323 in this study (Fig. S1) shows that the ICESat-derived Point F locations in 2004-2005 are close to the MEaSUREs GL in 1996, which gives us confidence that the 1996 GL is correct. The GL retreat rates based on ICESat-2-derived Point F locations and the 1996 MEaSUREs GL are 0.36-0.46 km yr^{-1} along the ice flowlines at the eastern flank of MUIS, while the highest retreat rate in this region calculated by Konrad et al. (2018) is 0.079 ± 0.029 km yr^{-1}. However, on the western flank of MUIS, the GL retreat rate from ICESat-2 between 1996 and 2020 is around 0.57 km yr^{-1}, at a similar magnitude to the highest retreat rate of 0.25 ± 0.099 km yr^{-1} predicted by Konrad et al. (2018). Konrad et al. (2018) did not map the GL location, instead, they calculated the GL migration rate based on a hydrostatic equilibrium assumption using CryoSat-2-derived surface elevation and the Bedmap-2 bed elevation at the MEaSUREs GL locations (Rignot et al., 2011). The bed elevation in MUIS GZ, however, has large uncertainties especially on MUIS due to the lack of airborne radar data coverage (Fig. S32 in Morlighem et al. (2020)), where the difference between BedMachine and Bedmap-2 bed elevations can be up to 1 km. Therefore, such an approach is likely to have large uncertainties in regions like MUIS,

https://doi.org/10.5194/tc-2022-129
Preprint. Discussion started: 13 July 2022

which might cause discrepancies with our GL retreat rates. For Track 841 GT1L (Fig. 4d), the modelled tidal phases are the opposite of the ICESat-2-derived elevation anomalies, although the identified Point F locations are close to the Sentinel-1a/b DInSAR-derived GL in 2018 by Mohajerani et al. (2021) (Fig. 2a). The reason for this tidal phase difference is possibly because the ice at the deep GZ cannot respond adequately in phase with ocean tides (Reeh et al., 2000).

Both the western and eastern flanks of the MUIS GZ showed ice velocity acceleration during 2007-2010 (Figs. 13a-b). This ice velocity acceleration was unlikely to be caused by iceberg calving events at the ice shelf front, because the sizes of individual iceberg calving events between 2005-2009 are all small-to-medium with an area below 25 km^2 (Qi et al., 2021). These small calving events should locate inside the "safety band" of the MUIS (Fürst et al., 2016; Reese et al., 2018), the region where mass loss will not cause major dynamic changes at the GZ. Therefore, a possible explanation for this discrepancy between ice velocity acceleration and small calving events might be ice dynamics. Studies have shown that MUIS has been losing an integrated mass of 93 Gt during the past four decades, equivalent to a sea-level rise of 0.3 mm (Rignot et al., 2019). The ice surface elevation at the fast-flowing region has also been decreasing significantly during the past two decades (Smith et al., 2020), similar to the negative surface elevation change between 2010-2019 in our study (Fig. 12). The western flank of the MUIS GZ is located at a retrograde bed slope (Fig. S4a), therefore current ice thinning trends might contribute a continuous GL retreat in future.

The large GL retreat of 11.95 ± 0.13 km from 1996-2021 at the MUIS West ice shelf is located at an ice plain with a low height above flotation (Fig.11d) with a high ice velocity (Fig. 9a) and small surface elevation change (Fig.12). In comparison, the observed GL migration here conflicts with the GL advance predicted in Konrad et al. (2018). Our results also reveal the existence of a tide-modulated ocean channel with a water depth deeper than 600 m below sea level (Figs. 9, 14 and S4d). Warm mCDW has been observed at the Sabrina Coast continental shelf in front of the TGIS (Fig. 1), and can reach the Totten Eastern Ice Shelf cavity through a deep trough to drive rapid basal melt (Fig. 8) (Greenbaum et al., 2015; Rintoul et al., 2016; Silvano et al., 2017). This poleward transport is possibly caused by a combination of wind forcing, decreased polynya activity and cyclonic eddies (Greene et al., 2017; Gwyther et al., 2014; Hirano et al., 2021). Similarly, the ocean heat transfer by mCDW to the MUIS depends on the nearby Dalton polynya activity and the flow route of Antarctic Slope Current (ASC) across the Dalton Rise (Gwyther et al., 2014). A low polynya activity and an overflow over the Dalton Rise will result in a strong inflow of warm water into the MUIS cavity. The newly discovered MUIS west ocean channel, which connects the MUIS West Ice Shelf and the Totten Eastern Ice Shelf, provides a route for mCDW to reach the MUIS West Ice Shelf from the neighboring Totten Eastern Ice Shelf cavity (green arrow in Figure 14). Similar to the mechanism proposed by Greenbaum et al. (2015) on the retreat of the Totten Eastern GZ, the GL retreat at the MUIS West Ice Shelf is possibly caused by the increased ice shelf basal melting due to ocean heat transferred through this ocean channel, especially in a region of high hydrostatic potential (Fig. 11d). If thinning continues, the GL will retreat to a retrograde bed slope just south of the current GL indicated by the white arrow in Figure 14, which has the potential to trigger a regional MISI. This will result in further GL migration and contribute to the destabilization of the MUIS sector in the future.

https://doi.org/10.5194/tc-2022-129
Preprint. Discussion started: 13 July 2022

While Sentinel-1a/b DInSAR interferograms show the existence of an ocean channel at the Totten Eastern Ice Shelf similar to the findings of Greenbaum et al. (2015), the channel width is highly correlated with ocean tide variations (Fig. 10a). In contrast to the prediction of a long-term channel widening caused by ice thinning in their study, the largest channel width observed in this study is 3.89 ± 0.13 km (Table S7), comparable to the ~4 km channel width measured in 2008-2012 by Greenbaum et al. (2015). In addition, Figure 8 shows that the Totten Eastern Ice Shelf ocean channel closed at low tide. If this short-term opening and closing was the case in 1996, it is likely that the 1996 MEaSUREs GL was accurate since the reconstructed tidal range from both the CATS2008 (orange vertical dotted line in Figure 10a) and FES2014 tidal models (Table S3) was low and the channel could be closed as a result.

As the weak underbelly of East Antarctica, Wilkes Land has been losing mass at accelerated rates due to warm water intrusion (Rignot et al., 2019; Pelle et al., 2020). Although extensive research has been carried out on the main glacier trunk of Totten Glacier Ice Shelf, our results show that not only the GL at the southern lobe of TGIS keeps retreating at a comparable rate to 1996-2013, other regions, including Totten East branch, MUIS and MUIS west, show pervasive GL retreats along the retrograde bed slopes at the fast-flowing regions. Moreover, an ocean channel at MUIS West discovered in this study can provide a pathway for ocean heat into the MUIS main ice shelf cavity. Although we are unable to identify the exact time stamps of the GL retreat during the past two decades for MUIS, multiple lines of evidence show that MUIS and MUIS West are susceptible to potential MISI and are currently contributing to sea-level rise.

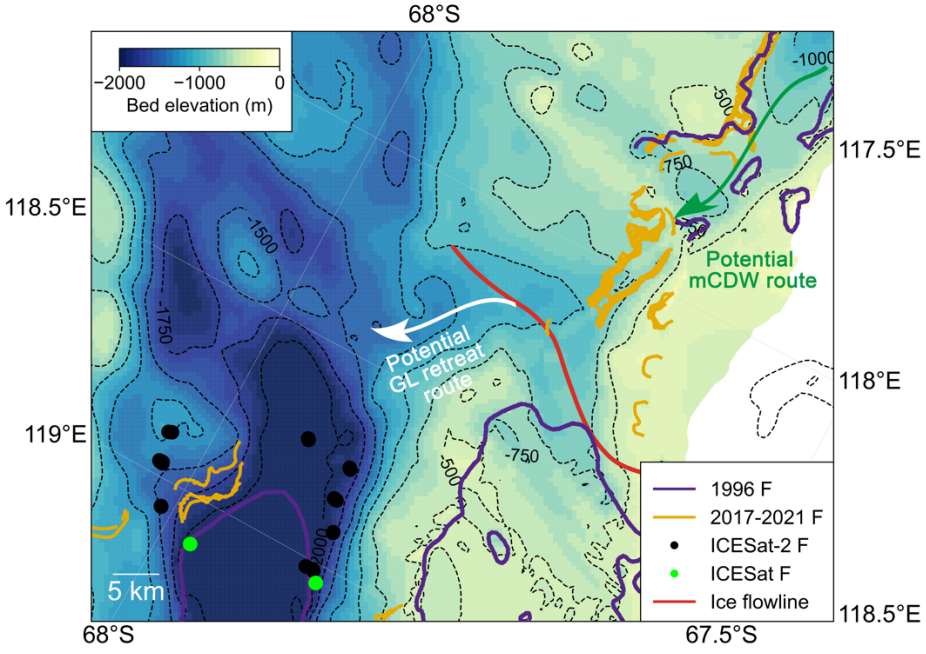

Figure 14. The potential grounding line retreat route at the Moscow University western ice shelf along the retrograde bed slope is shown by the white arrow into the main glacier trunk of Moscow University Ice Shelf. The potential mCDW route from Totten

https://doi.org/10.5194/tc-2022-129
Preprint. Discussion started: 13 July 2022

Eastern Ice Shelf is marked by a green arrow. All the map features are overlaid on the BedMachine bed elevation (Morlighem et al., 2020).

5 Conclusion

By combining Sentinel-1a/b DInSAR interferograms and ICESat-2 laser altimetry data between 1996 and 2020, we found pervasive GL retreats along the ice plains at the glacier central trunks of Totten and Moscow University glaciers, which drain a large portion of the marine-based Aurora Subglacial Basin in East Antarctica. The GL retreated 9.37 ± 1.04 km and 13.85 ± 0.08 km at the eastern and western flanks of MUIS main glacier trunk, respectively. Meanwhile, the GL retreated 5.95 ± 0.75 km and 3.51 ± 0.49 km at the TGIS East branch and the southern lobe of the TGIS main glacier trunk, respectively. The GL retreats are concentrated along fast-flowing regions with observed high thinning rates over the past 10 years, indicating a dynamical mass imbalance, likely related to the presence of warm mCDW in this region. GL retreats at the MUIS and Totten East branch are along retrograde bed slopes, accompanied by ice velocity acceleration and negative surface elevation change, indicating that regional MISI is likely underway. The analysis of Sentinel-1a/b DInSAR interferogram time series also discovers a tide-modulated ocean channel located at MUIS West. The opening of this channel connects the two separate MUIS and TGIS systems, which might open a pathway for the warm mCDW to enter the MUIS west ice shelf cavity from the Totten Eastern Ice shelf cavity. This could facilitate further GL retreat at MUIS west along a retrograde bed slope and merge into the main glacier trunk of MUIS in the future. Despite these GL migrations, our study finds that the Totten eastern ocean channel has not further expanded as suggested by Greenbaum et al. (2015), and its width is positively correlated with the ocean tidal range.

This paper is the first comprehensive investigation of both short-term and long-term GL changes on Totten and Moscow University Glaciers. Although we are unable to identify the exact time stamps of GL retreats, the findings offer new insights into the current GL and ice sheet instability in Wilkes Land, a region that has the potential to make a significant contribution to future sea-level rise. Additionally, this study highlights the importance of using a combination of different Earth observation techniques in monitoring the GL locations, especially in separating short-term tidal variability from the long-term GL migrations. With the advent of more ICESat-2 data in coming years as well as the new NASA-ISRO SAR (NISAR) Mission planned for January 2023, a routine monitoring of this critical region with improved coverage will be possible.

Data availability

The ICESat-2 and ICESat surface elevation data used in this study are available from the National Snow and Ice Data Center (NSIDC). The CryoSat-2 Swath mode thematic point product was processed by CryoTEMPOEOLIS (https://www.cryotempo-eolis.org) and is distributed by the European Space Agency (ESA) (https://sciencepds.cryosat.esa.int/). The Sentinel-1a/b data is provided by the ESA and is accessible from the Alaska

Satellite Facility (ASF) via the ASF API (https://asf.alaska.edu/api/). The grounding line data produced in this study will be available via a DOI generated at the University of Bristol data repository, data.bris.

Author contribution

TL designed the study, produced the results, and wrote the paper. GJD assisted with DInSAR processing. SJC produced the CryoSat-2 elevation change. JLB conceived the study and contributed to the interpretation of the results and paper writing. All authors commented on the manuscript.

Competing interests

The authors declare that they have no conflict of interest.

Acknowledgements

Tian Li received funding from the China Scholarship Council (CSC)–University of Bristol joint-funded PhD scholarship. Jonathan L. Bamber and Stephen J. Chuter received funding from the European Research Council (GlobalMass; grant no. 694188). Stephen J. Chuter also received funding from the European Space Agency (ESA) as part of the Climate Change Initiative (CCI) fellowship (ESA ESRIN/Contract No. 4000133466/20/I/NB). Jonathan L. Bamber also received funding from the German Federal Ministry of Education and Research (BMBF) in the framework of the international future lab AI4EO (grant no. 01DD20001). We thank Michiel van den Broeke and Peter Kuipers Munneke for providing the RACMO 2.3 data. We thank Chad A. Greene and Bernd Scheuchl for providing valuable comments on this study.

References

Adusumilli, S., Fricker, H. A., Medley, B., Padman, L. and Siegfried, M. R.: Interannual variations in meltwater input to the Southern Ocean from Antarctic ice shelves, Nat. Geosci., 13(9), 616–620, doi:10.1038/s41561-020-0616-z, 2020.

Aitken, A. R. A., Roberts, J. L., Van Ommen, T. D., Young, D. A., Golledge, N. R., Greenbaum, J. S., Blankenship, D. D. and Siegert, M. J.: Repeated large-scale retreat and advance of Totten Glacier indicated by inland bed erosion, Nature, doi:10.1038/nature17447, 2016.

Bamber, J. L., Gomez-Dans, J. L. and Griggs, J. A.: A new 1 km digital elevation model of the Antarctic derived from combined satellite radar and laser data - Part 1: Data and methods, Cryosphere, 3(1), 101–111, doi:10.5194/TC-3-101-2009, 2009a.

Bamber, J. L., Riva, R. E. M., Vermeersen, B. L. A. and Lebrocq, A. M.: Reassessment of the potential sea-level rise from a

collapse of the west antarctic ice sheet, Science (80-.)., doi:10.1126/science.1169335, 2009b.

Borsa, A. A., Moholdt, G., Fricker, H. A. and Brunt, K. M.: A range correction for ICESat and its potential impact on ice-sheet mass balance studies, Cryosphere, 8(2), 345–357, doi:10.5194/TC-8-345-2014, 2014.

Brancato, V., Rignot, E., Milillo, P., Morlighem, M., Mouginot, J., An, L., Scheuchl, B., Jeong, S., Rizzoli, P., Bueso Bello, J. L. and Prats-Iraola, P.: Grounding Line Retreat of Denman Glacier, East Antarctica, Measured With COSMO-SkyMed Radar Interferometry Data, Geophys. Res. Lett., 47(7), doi:10.1029/2019GL086291, 2020.

Brunt, K. M., Fricker, H. A., Padman, L. and O'Neel, S.: ICESat-derived Grounding Zone for Antarctic Ice Shelves, , doi:https://doi.org/10.7265/N5CF9N19, 2010a.

Brunt, K. M., Fricker, H. A., Padman, L., Scambos, T. A. and O'Neel, S.: Mapping the grounding zone of the Ross Ice Shelf, Antarctica, using ICESat laser altimetry, Ann. Glaciol., doi:10.3189/172756410791392790, 2010b.

Brunt, K. M., Fricker, H. A. and Padman, L.: Analysis of ice plains of the Filchner-Ronne Ice Shelf, Antarctica, using ICESat laser altimetry, J. Glaciol., doi:10.3189/002214311798043753, 2011.

Chuter, S. J. and Bamber, J. L.: Antarctic ice shelf thickness from CryoSat-2 radar altimetry, Geophys. Res. Lett., doi:10.1002/2015GL066515, 2015.

Chuter, S. J., Zammit-Mangion, A., Rougier, J., Dawson, G. and Bamber, J. L.: Mass evolution of the Antarctic Peninsula over the last 2 decades from a joint Bayesian inversion, Cryosph., 16(4), 1349–1367, doi:10.5194/TC-16-1349-2022, 2022.

Dawson, G. J. and Bamber, J. L.: Antarctic Grounding Line Mapping From CryoSat-2 Radar Altimetry, Geophys. Res. Lett., 44(23), 11,886-11,893, doi:10.1002/2017GL075589, 2017.

Depoorter, M. A., Bamber, J. L., Griggs, J. A., Lenaerts, J. T. M., Ligtenberg, S. R. M., Van Den Broeke, M. R. and Moholdt, G.: Calving fluxes and basal melt rates of Antarctic ice shelves, Nature, 502(7469), 89–92, doi:10.1038/nature12567, 2013.

ESA: Antarctic Ice Sheet Climate Change Initiative, Grounding Line Locations for the Denman and Totten Glaciers, Antarctica, 1996–2015 v1.0, Cent. Environ. Data Anal., 2017.

Fricker, H. A. and Padman, L.: Ice shelf grounding zone structure from ICESat laser altimetry, Geophys. Res. Lett., doi:10.1029/2006GL026907, 2006.

Fricker, H. A., Coleman, R., Padman, L., Scambos, T. A., Bohlander, J. and Brunt, K. M.: Mapping the grounding zone of the Amery Ice Shelf, East Antarctica using InSAR, MODIS and ICESat, Antarct. Sci., doi:10.1017/S095410200999023X, 2009.

Fürst, J. J., Durand, G., Gillet-Chaulet, F., Tavard, L., Rankl, M., Braun, M. and Gagliardini, O.: The safety band of

Antarctic ice shelves, Nat. Clim. Chang., 6(5), 479–482, doi:10.1038/nclimate2912, 2016.

Gardner, A. S., Moholdt, G., Scambos, T., Fahnstock, M., Ligtenberg, S., van den Broeke, M. and Nilsson, J.: Increased West Antarctic and unchanged East Antarctic ice discharge over the last 7 years, Cryosph., 12(2), 521–547, doi:10.5194/tc-12-521-2018, 2018.

Gardner, A. S., Fahnestock, M. A. and Scambos, T. A.: MEaSUREs ITS_LIVE Landsat Image-Pair Glacier and Ice Sheet Surface Velocities: Version 1, Data Arch. Natl. Snow Ice Data Cent., Accessed Dec-2020, doi:10.5067/6II6VW8LLWJ7, 2019.

Goodwin, I. D.: Snow accumulation and surface topography in the katabatic zone of Eastern Wilkes Land, Antarctica, Antarct. Sci., 2(3), 235–242, doi:10.1017/S0954102090000323, 1990.

Gourmelen, N., Escorihuela, M. J., Shepherd, A., Foresta, L., Muir, A., Garcia-Mondéjar, A., Roca, M., Baker, S. G. and Drinkwater, M. R.: CryoSat-2 swath interferometric altimetry for mapping ice elevation and elevation change, Adv. Sp. Res., 62(6), 1226–1242, doi:10.1016/j.asr.2017.11.014, 2018.

Gray, L., Burgess, D., Copland, L., Dunse, T., Langley, K. and Moholdt, G.: A revised calibration of the interferometric mode of the CryoSat-2 radar altimeter improves ice height and height change measurements in western Greenland, Cryosph., 11(3), 1041–1058, doi:10.5194/tc-11-1041-2017, 2017.

Greenbaum, J. S., Blankenship, D. D., Young, D. A., Richter, T. G., Roberts, J. L., Aitken, A. R. A., Legresy, B., Schroeder, D. M., Warner, R. C., Van Ommen, T. D. and Siegert, M. J.: Ocean access to a cavity beneath Totten Glacier in East Antarctica, Nat. Geosci., doi:10.1038/ngeo2388, 2015.

Greene, C. A., Blankenship, D. D., Gwyther, D. E., Silvano, A. and Van Wijk, E.: Wind causes Totten Ice Shelf melt and acceleration, Sci. Adv., doi:10.1126/sciadv.1701681, 2017.

Gwyther, D. E., Galton-Fenzi, B. K., Hunter, J. R. and Roberts, J. L.: Simulated melt rates for the Totten and Dalton ice shelves, Ocean Sci., 10(3), 267–279, doi:10.5194/os-10-267-2014, 2014.

Hirano, D., Mizobata, K., Sasaki, H., Murase, H., Tamura, T. and Aoki, S.: Poleward eddy-induced warm water transport across a shelf break off Totten Ice Shelf, East Antarctica, Commun. Earth Environ., 2(1), 153, doi:10.1038/s43247-021-00217-4, 2021.

Hofton, M. A., Luthcke, S. B. and Blair, J. B.: Estimation of ICESat intercampaign elevation biases from comparison of lidar data in East Antarctica, Geophys. Res. Lett., 40(21), 5698–5703, doi:10.1002/2013GL057652, 2013.

Howat, I. M., Porter, C., Smith, B. E., Noh, M. J. and Morin, P.: The reference elevation model of antarctica, Cryosphere, doi:10.5194/tc-13-665-2019, 2019.

Joughin, I., Smith, B. E. and Medley, B.: Marine ice sheet collapse potentially under way for the Thwaites Glacier Basin,

West Antarctica, Science (80-.)., 344(6185), 735–738, doi:10.1126/science.1249055, 2014.

Khazendar, A., Schodlok, M. P., Fenty, I., Ligtenberg, S. R. M., Rignot, E. and van den Broeke, M. R.: Observed thinning of Totten Glacier is linked to coastal polynya variability, Nat. Commun., 4(1), 2857, doi:10.1038/ncomms3857, 2013.

Konrad, H., Shepherd, A., Gilbert, L., Hogg, A. E., McMillan, M., Muir, A. and Slater, T.: Net retreat of Antarctic glacier grounding lines, Nat. Geosci., 11(4), 258–262, doi:10.1038/s41561-018-0082-z, 2018.

Kuipers Munneke, P., Ligtenberg, S. R. M., Noël, B. P. Y., Howat, I. M., Box, J. E., Mosley-Thompson, E., McConnell, J. R., Steffen, K., Harper, J. T., Das, S. B. and Van Den Broeke, M. R.: Elevation change of the Greenland Ice Sheet due to surface mass balance and firn processes, 1960-2014, Cryosphere, doi:10.5194/tc-9-2009-2015, 2015.

Li, T., Dawson, G. J., Chuter, S. J. and Bamber, J. L.: Mapping the grounding zone of Larsen C Ice Shelf, Antarctica, from ICESat-2 laser altimetry, Cryosph., doi:10.5194/tc-14-3629-2020, 2020.

Li, T., Dawson, G. J., Chuter, S. J. and Bamber, J. L.: A high-resolution Antarctic grounding zone product from ICESat-2 laser altimetry, Earth Syst. Sci. Data, 14(2), 535–557, doi:10.5194/ESSD-14-535-2022, 2022.

Li, X., Rignot, E., Morlighem, M., Mouginot, J. and Scheuchl, B.: Grounding line retreat of Totten Glacier, East Antarctica, 1996 to 2013, Geophys. Res. Lett., doi:10.1002/2015GL065701, 2015.

Li, X., Rignot, E., Mouginot, J. and Scheuchl, B.: Ice flow dynamics and mass loss of Totten Glacier, East Antarctica, from 1989 to 2015, Geophys. Res. Lett., 43(12), 6366–6373, doi:10.1002/2016GL069173, 2016.

Lyard, F. H., Allain, D. J., Cancet, M., Carrère, L. and Picot, N.: FES2014 global ocean tide atlas: Design and performance, Ocean Sci., 17(3), 615–649, doi:10.5194/OS-17-615-2021, 2021.

Markus, T., Neumann, T., Martino, A., Abdalati, W., Brunt, K., Csatho, B., Farrell, S., Fricker, H., Gardner, A., Harding, D., Jasinski, M., Kwok, R., Magruder, L., Lubin, D., Luthcke, S., Morison, J., Nelson, R., Neuenschwander, A., Palm, S., Popescu, S., Shum, C. K., Schutz, B. E., Smith, B., Yang, Y. and Zwally, J.: The Ice, Cloud, and land Elevation Satellite-2 (ICESat-2): Science requirements, concept, and implementation, Remote Sens. Environ., doi:10.1016/j.rse.2016.12.029, 2017.

Melchior Van Wessem, J., Jan Van De Berg, W., Noël, B. P. Y., Van Meijgaard, E., Amory, C., Birnbaum, G., Jakobs, C. L., Krüger, K., Lenaerts, J. T. M., Lhermitte, S., Ligtenberg, S. R. M., Medley, B., Reijmer, C. H., Van Tricht, K., Trusel, L. D., Van Ulft, L. H., Wouters, B., Wuite, J. and Van Den Broeke, M. R.: Modelling the climate and surface mass balance of polar ice sheets using RACMO2 - Part 2: Antarctica (1979-2016), Cryosphere, 12(4), 1479–1498, doi:10.5194/tc-12-1479-2018, 2018.

Milillo, P., Rignot, E., Mouginot, J., Scheuchl, B., Morlighem, M., Li, X. and Salzer, J. T.: On the Short-term Grounding Zone Dynamics of Pine Island Glacier, West Antarctica, Observed With COSMO-SkyMed Interferometric Data, Geophys.

Res. Lett., 44(20), 10,436-10,444, doi:10.1002/2017GL074320, 2017.

Milillo, P., Rignot, E., Rizzoli, P., Scheuchl, B., Mouginot, J., Bueso-Bello, J. L., Prats-Iraola, P. and Dini, L.: Rapid glacier retreat rates observed in West Antarctica, Nat. Geosci., 15(1), 48–53, doi:10.1038/s41561-021-00877-z, 2022.

Mohajerani, Y., Jeong, S., Scheuchl, B., Velicogna, I., Rignot, E. and Milillo, P.: Automatic delineation of glacier grounding lines in differential interferometric synthetic-aperture radar data using deep learning, Sci. Rep., 11(1), 4992, doi:10.1038/s41598-021-84309-3, 2021.

Morlighem, M.: MEaSUREs BedMachine Antarctica, Version 2, NASA Natl. Snow Ice Data Cent. Distrib. Act. Arch. Cent., doi:https://doi.org/10.5067/E1QL9HFQ7A8M, 2020.

Morlighem, M., Rignot, E., Binder, T., Blankenship, D., Drews, R., Eagles, G., Eisen, O., Ferraccioli, F., Forsberg, R., Fretwell, P., Goel, V., Greenbaum, J. S., Gudmundsson, H., Guo, J., Helm, V., Hofstede, C., Howat, I., Humbert, A., Jokat, W., Karlsson, N. B., Lee, W. S., Matsuoka, K., Millan, R., Mouginot, J., Paden, J., Pattyn, F., Roberts, J., Rosier, S., Ruppel, A., Seroussi, H., Smith, E. C., Steinhage, D., Sun, B., Broeke, M. R. va. den, Ommen, T. D. va., Wessem, M. van and Young, D. A.: Deep glacial troughs and stabilizing ridges unveiled beneath the margins of the Antarctic ice sheet, Nat. Geosci., 13(2), 132–137, doi:10.1038/s41561-019-0510-8, 2020.

Mouginot, J., Rignot, E., Scheuchl, B. and Millan, R.: Comprehensive Annual Ice Sheet Velocity Mapping Using Landsat-8, Sentinel-1, and RADARSAT-2 Data, Remote Sens., 9(4), 364, doi:10.3390/RS9040364, 2017a.

Mouginot, J., Scheuchl, B. and E. Rignot: MEaSUREs Annual Antarctic Ice Velocity Maps 2005-2017, Version 1. Boulder, Colorado USA, , doi:https://doi.org/10.5067/9T4EPQXTJYW9, 2017b.

Nitsche, F. O., Porter, D., Williams, G., Cougnon, E. A., Fraser, A. D., Correia, R. and Guerrero, R.: Bathymetric control of warm ocean water access along the East Antarctic Margin, Geophys. Res. Lett., 44(17), 8936–8944, doi:10.1002/2017GL074433, 2017.

Padman, L., Fricker, H. A., Coleman, R., Howard, S. and Erofeeva, L.: A new tide model for the Antarctic ice shelves and seas, Ann. Glaciol., 34, 247–254, doi:10.3189/172756402781817752, 2002.

Pelle, T., Morlighem, M. and McCormack, F. S.: Aurora Basin, the Weak Underbelly of East Antarctica, Geophys. Res. Lett., 47(9), e2019GL086821, doi:10.1029/2019GL086821, 2020.

Pelle, T., Morlighem, M., Nakayama, Y. and Seroussi, H.: Widespread Grounding Line Retreat of Totten Glacier, East Antarctica, Over the 21st Century, Geophys. Res. Lett., 48(17), e2021GL093213, doi:10.1029/2021GL093213, 2021.

Pritchard, H. D., Ligtenberg, S. R. M., Fricker, H. A., Vaughan, D. G., Van Den Broeke, M. R. and Padman, L.: Antarctic ice-sheet loss driven by basal melting of ice shelves, Nature, 484(7395), 502–505, doi:10.1038/nature10968, 2012.

Qi, M., Liu, Y., Liu, J., Cheng, X., Lin, Y., Feng, Q., Shen, Q. and Yu, Z.: A 15-year circum-Antarctic iceberg calving

dataset derived from continuous satellite observations, Earth Syst. Sci. Data, 13(9), 4583–4601, doi:10.5194/essd-13-4583-2021, 2021.

Reeh, N., Mayer, C., Olesen, O. B., Christensen, E. L. and Thomsen, H. H.: Tidal movement of Nioghalvfjerdsfjorden glacier, northeast Greenland: Observation and modelling, Ann. Glaciol., 31, 111–117, doi:10.3189/172756400781820408, 2000.

Reese, R., Gudmundsson, G. H., Levermann, A. and Winkelmann, R.: The far reach of ice-shelf thinning in Antarctica, Nat. Clim. Chang., 8(1), 53–57, doi:10.1038/s41558-017-0020-x, 2018.

Rignot, E., Mouginot, J. and Scheuchl, B.: Antarctic grounding line mapping from differential satellite radar interferometry, Geophys. Res. Lett., doi:10.1029/2011GL047109, 2011.

Rignot, E., Mouginot, J. and Scheuchl, B.: MEaSUREs Antarctic Grounding Line from Differential Satellite Radar Interferometry, Version 2. Boulder, Colorado USA, , doi:https://doi.org/10.5067/IKBWW4RYHF1Q, 2016.

Rignot, E., Mouginot, J. and Scheuchl, B.: MEaSUREs InSAR-Based Antarctica Ice Velocity Map, Version 2. Boulder, Colorado USA, , doi:https://doi.org/10.5067/D7GK8F5J8M8R, 2017.

Rignot, E., Mouginot, J., Scheuchl, B., Van Den Broeke, M., Van Wessem, M. J. and Morlighem, M.: Four decades of Antarctic ice sheet mass balance from 1979–2017, Proc. Natl. Acad. Sci. U. S. A., 116(4), 1095–1103, doi:10.1073/pnas.1812883116, 2019.

Rintoul, S. R., Silvano, A., Pena-Molino, B., Van Wijk, E., Rosenberg, M., Greenbaum, J. S. and Blankenship, D. D.: Ocean heat drives rapid basal melt of the Totten Ice Shelf, Sci. Adv., doi:10.1126/sciadv.1601610, 2016.

Sandwell, D., Mellors, R., Tong, X., Wei, M. and Wessel, P.: Open radar interferometry software for mapping surface Deformation, Eos, Trans. Am. Geophys. Union, 92(28), 234–234, doi:10.1029/2011EO280002, 2011.

Scambos, T. A., Haran, T. M., Fahnestock, M. A., Painter, T. H. and Bohlander, J.: MODIS-based Mosaic of Antarctica (MOA) data sets: Continent-wide surface morphology and snow grain size, Remote Sens. Environ., doi:10.1016/j.rse.2006.12.020, 2007.

Scheick, J.: icepyx: Python tools for obtaining and working with ICESat-2 data, , doi:https://github.com/icesat2py/icepyx, 2019.

Schoof, C.: Ice sheet grounding line dynamics: Steady states, stability, and hysteresis, J. Geophys. Res. Earth Surf., 112(3), doi:10.1029/2006JF000664, 2007.

Shepherd, A., Ivins, E., Rignot, E., Smith, B., Van Den Broeke, M., Velicogna, I., Whitehouse, P., Briggs, K., Joughin, I., Krinner, G., Nowicki, S., Payne, T., Scambos, T., Schlegel, N., Geruo, A., Agosta, C., Ahlstrøm, A., Babonis, G., Barletta, V., Blazquez, A., Bonin, J., Csatho, B., Cullather, R., Felikson, D., Fettweis, X., Forsberg, R., Gallee, H., Gardner, A.,

Gilbert, L., Groh, A., Gunter, B., Hanna, E., Harig, C., Helm, V., Horvath, A., Horwath, M., Khan, S., Kjeldsen, K. K., Konrad, H., Langen, P., Lecavalier, B., Loomis, B., Luthcke, S., McMillan, M., Melini, D., Mernild, S., Mohajerani, Y., Moore, P., Mouginot, J., Moyano, G., Muir, A., Nagler, T., Nield, G., Nilsson, J., Noel, B., Otosaka, I., Pattle, M. E., Peltier, W. R., Pie, N., Rietbroek, R., Rott, H., Sandberg-Sørensen, L., Sasgen, I., Save, H., Scheuchl, B., Schrama, E., Schröder, L., Seo, K. W., Simonsen, S., Slater, T., Spada, G., Sutterley, T., Talpe, M., Tarasov, L., Van De Berg, W. J., Van Der Wal, W., Van Wessem, M., Vishwakarma, B. D., Wiese, D. and Wouters, B.: Mass balance of the Antarctic Ice Sheet from 1992 to 2017, Nature, doi:10.1038/s41586-018-0179-y, 2018.

Silvano, A., Rintoul, S. R., Peña-Molino, B. and Williams, G. D.: Distribution of water masses and meltwater on the continental shelf near the Totten and Moscow University ice shelves, J. Geophys. Res. Ocean., 122(3), 2050–2068, doi:10.1002/2016JC012115, 2017.

Smith, B., Fricker, H. A., Holschuh, N., Gardner, A. S., Adusumilli, S., Brunt, K. M., Csatho, B., Harbeck, K., Huth, A., Neumann, T., Nilsson, J. and Siegfried, M. R.: Land ice height-retrieval algorithm for NASA's ICESat-2 photon-counting laser altimeter, Remote Sens. Environ., 233, doi:10.1016/j.rse.2019.111352, 2019.

Smith, B., Fricker, H. A., Gardner, A. S., Medley, B., Nilsson, J., Paolo Nicholas Holschuh, F. S., Adusumilli, S., Brunt, K., Csatho, B., Harbeck, K., Markus, T., Neumann, T., Siegfried, M. R. and Jay Zwally, H.: Pervasive ice sheet mass loss reflects competing ocean and atmosphere processes, Science (80-.)., 368(6496), 1239–1242, doi:10.1126/science.aaz5845, 2020.

Smith, B., Fricker, H. A., Gardner, A., Siegfried, M. R., Adusumilli, S., Csathó, B. M., Holschuh, N., Nilsson, J., Paolo, F. S. and Team, and the Ices.-2 S.: ATLAS/ICESat-2 L3A Land Ice Height, Version 4, NASA Natl. Snow Ice Data Cent. Distrib. Act. Arch. Cent., doi:https://doi.org/10.5067/ATLAS/ATL06.004, 2021.